Lab on a Chip

PAPER

View Article Online
View Journal | View Issue

Cite this: *Lab Chip*, 2021, **21**, 4177

A dynamic microscale mid-throughput fibrosis model to investigate the effects of different ratios of cardiomyocytes and fibroblasts†

Andrea Mainardi, [abc] Francesca Carminati,[ab] Giovanni Stefano Ugolini,[a] Paola Occhetta, [bd] Giuseppe Isu,[b] Diana Robles Diaz,[a] Gregory Reid, [ac] Roberta Visone, [b] Marco Rasponi ‡[b] and Anna Marsano ‡*[a]

Cardiac fibrosis is a maladaptive remodeling of the myocardium hallmarked by contraction impairment and excessive extracellular matrix deposition (ECM). The disease progression, nevertheless, remains poorly understood and present treatments are not capable of controlling the scarring process. This is partly due to the absence of physiologically relevant, easily operable, and low-cost *in vitro* models, which are of the utmost importance to uncover pathological mechanisms and highlight possible targets for anti-fibrotic therapies. In classic models, fibrotic features are usually obtained using substrates with scar mimicking stiffness and/or supplementation of morphogens such as transforming growth factor β1 (TGF-β1). Qualities such as the interplay between activated fibroblasts (FBs) and cardiomyocytes (CMs), or the mechanically active, three-dimensional (3D) environment, are, however, neglected or obtained at the expense of the number of experimental replicates achievable. To overcome these shortcomings, we engineered a micro-physiological system (MPS) where multiple 3D cardiac micro-tissues can be subjected to cyclical stretching simultaneously. Up to six different biologically independent samples are incorporated in a single device, increasing the experimental throughput and paving the way for higher yielding drug screening campaigns. The newly developed MPS was used to co-culture different ratios of neonatal rat CMs and FBs, investigating the role of CMs in the modulation of fibrosis traits, without the addition of morphogens, and in soft substrates. The expression of contractile stress fibers and of degradative enzymes, as well as the deposition of fibronectin and type I collagen were superior in microtissues with a low amount of CMs. Moreover, high CM-based microconstructs simulating a ratio similar to that of healthy tissues, even if subjected to both cyclic stretch and TGF-β1, did not show any of the investigated fibrotic signs, indicating a CM fibrosis modulating effect. Overall, this *in vitro* fibrosis model could help to uncover new pathological aspects studying, with mid-throughput and in a mechanically active, physiologically relevant environment, the crosstalk between the most abundant cell types involved in fibrosis.

Received 4th February 2021,
Accepted 3rd May 2021

DOI: 10.1039/d1lc00092f

rsc.li/loc

Introduction

Cardiac fibrosis is a maladaptive pathological remodelling that usually follows myocardial infarction (MI) leading to cardiac dysfunction and enhanced risk of arrythmias.[1] Quiescent cardiac fibroblasts (FBs), activated by the wound healing cascade, switch their phenotype into myofibroblasts, increasing the expression levels of contractile proteins such as α-smooth muscle actin (αSMA), enhancing the deposition of ECM proteins (*e.g.* type-I collagen and fibronectin), and endorsing a profibrotic environment.[2,3] This adaptive course prevents the rupture of the ventricular wall; however, it ultimately results in tissue stiffening and altered current conductivity that all together impair the normal heart function.[4]

Therapeutic solutions under study generally aim at increasing the self-healing properties of cardiomyocytes and/or foster angiogenic processes.[5,6] Only a few research studies directly focused on the fibrotic processes, inhibiting key upregulated signalling pathways such as transforming growth factor beta (TGF-β) or connective tissue growth factor.[7,8] Consequently, there are no established anti-fibrotic

[a] *Departments of Biomedicine and Surgery, University Basel and University Hospital Basel, Hebelstrasse 20, CH-4031 Basel, Switzerland. E-mail: Anna.Marsano@usb.ch; Fax: +41 61 265 3990; Tel: +41 61 265 2979*
[b] *Department of Electronics, Information and Bioengineering, Politecnico di Milano, Milano, Italy*
[c] *Department of Biomedical Engineering, University of Basel, Allschwil, Switzerland*
[d] *BiomimX S.r.l., Via Giovanni Durando 38/A, 20158 Milano, Italy*

† Electronic supplementary information (ESI) available. See DOI: 10.1039/d1lc00092f

‡ Equally contributing authors.

treatments in the current clinical setting. This shortage might correlate with the lack of representative and predictive models allowing *ad hoc* investigations of fibrosis.

Animal models of myocardial infarction have often been employed for studying the fundamental mechanisms underlying fibrosis[9,10] but the complexity of such models does not allow the role and interplay of individual cues (*e.g.* altered mechanics, dysregulated cellular populations, inflammation, *etc.*) to be investigated in the pathological onset and evolution.

Hence, *in vitro* models to investigate scar formation mechanisms with sufficient operational ease, low cost, and high experimental throughput[11] are highly desirable.

Classic plasticware-based two-dimensional (2D) rigid substrates are, however, inadequate as they cause spontaneous fibroblast differentiation into myofibroblasts due to their non-physiological stiffness.[11]

The employment of hydrogel micropatterns featuring mechanical properties close to the stiffness of the post-infarction myocardium allowed fibrotic traits (such as αSMA expression, increased fibronectin deposition, and fibroblast migration towards more rigid areas) to be regulated although still in a 2D environment.[4] Three-dimensional (3D) fibrosis models have been used to investigate the effects of fibrotic signals and mechanical stimulation ranges on the myofibroblasts' persistence and evolution,[1,12,13] showing to be superior to 2D culture systems. Most often however, they still incorporate a single cell type (*i.e.* FBs), making it impossible to address the complex intercellular interactions that distinguish the fibrotic process.[1]

Indeed, key aspects such as the cellular type,[14] age,[15] origin,[16] and stage of differentiation, as well as the substrate composition and stiffness[14] were all proved to be highly relevant.

CM and FB interactions, for instance, were shown to be key not only for the comprehension of homeostasis and pathological conditions, in particular arrythmia, fibrosis, and hypertrophy,[10] but also in the determination of the effect of ECM alterations.[17] CMs seem to have protective properties, hindering the scar formation process led by activated FBs and thus making their incorporation instrumental in studying a possible cross-talk with activated FBs.[16,18] Rupert *et al.*[19] investigated the effects of different percentages (from 5 to 15%) of FBs on the electromechanics performance of 3D cardiac constructs, showing that addition of a superior number of FBs, either preactivated or not by TGF-β1 supplementation, negatively affected the CMs' functionality.[19] Van Spreeuwel *et al.* supported these findings, demonstrating that percentages of FBs greater than 50% caused a significant drop in the beating frequency and contraction force of cardiac microtissues *in vitro*. Notably, the contraction force was not affected by the simple increase of the collagen content in the microtissues mimicking the augmented stiffness of fibrotic myocardium.[17] Similar results were obtained adopting both FBs and CMs mixed in a fixed ratio (1 : 1 (ref. 11) or 10 : 3 (ref. 15)) to obtain contractile tissues. While the majority of the proposed models relied on the sole supplementation of the pro-fibrotic factor TGF-β1 as a fibrosis inductor, active supplementation of mechanical stimuli was demonstrated to provide better physiological mimicry.[12]

In vitro models based on microfluidic organ/tissue-on-chips or micro-physiological systems (MPSs) offer the possibility to better recapitulate *in vivo* occurring patho-physiological processes. MPSs allow great control over the experimental environment, easing both fundamental mechanistic investigation and drug screening processes,[20] while allowing incorporation of different compartments[21] and mechanical actuators.[20,22] Mimicking of myocardial beating through an MPS, for instance, was demonstrated by our group to advance the maturation and the contractile properties of cardiac microconstructs, leading to a more representative heart model.[22] Moreover, using the same single chamber device, we proved that cyclic uniaxial stimulation of 3D cardiac FB-laden fibrin gels can, alone, induce some of the key steps of scar formation usually achieved through the supplementation of TGF-β1.[12] This led to a model with limited confounding chemical factors and increased aptness for drug screening purposes.

The adequacy of MPSs in studying fibrotic features was, moreover, specifically proved by Mastikhina *et al.*[23]

Current MPSs, therefore, respond to the need for more representative *in vitro* organ and disease models.[24,25] Since MPSs are often constituted by a culture single chamber, the experimental yield achievable is heavily restricted, ultimately affecting their usability as extensive drug screening tools.[26] Even devices with a higher throughput are often based on the repetition, in an array fashion, of a single platform unit,[27] without a net increase of the operational ease. The low experimental throughput is more evident when mechanically active parts are present, complicating the overall device layout and requiring numerous inlet and outlets ports for an adequate function.

We previously demonstrated how multiple biologically independent 3D cardiac microtissues can be cultured in a novel device layout through a single injection. However, this layout was not compatible with the application of dynamic mechanical stimulation.[28]

For cardiac disease application, therefore, it is still an open challenge to generate a microfluidic-based 3D system capable of providing adequate mechanical stimuli, the necessary cell–cell interactions and microenvironmental conditions, and maintaining a sufficiently high throughput.

Addressing this deficit, we here developed a microfluidic device consisting of multiple chambers equipped with a mechanically active and finely tuneable 3D microenvironment to recapitulate some of the representative steps of cardiac fibrosis *in vitro*. In particular, we hypothesized that the presence of functional CMs could reduce the percentage of activated FBs and, therefore, hinder the triggering of a fibrotic process.

The role of CMs in dampening the onset of fibrosis traits was investigated through their coculture with different percentages of FBs when exposed to mechanical stretching or to the supplementation of the pro-fibrotic factor TGF-β1.

Results

Device concept

The proposed device was conceived to provide a controlled mechanical stimulation (*i.e.* uniaxial strain) to multiple 3D micro-constructs in independent culture chambers uniting features previously belonging to different models.[20,22,29] To increase the number of independent replicates, doormat-like valves were introduced to separate the individual culture chambers. This technology allowed a simultaneous seeding of the micro-engineered tissues and a tightly-sealed environment during their culture,[30] leading to higher experimental throughput compared to previously established systems.[12,22]

The device, realized in polydimethylsiloxane (PDMS), is composed of four layers (Fig. 1a): (i) top chamber, (ii) thin membrane, (iii) doormat valve layer, and (iv) pneumatic chamber layer.

The top chamber is constituted by six different culture chambers. Each chamber is organized in a central cell channel separated by two rows of overhanging posts from two culture medium channels.

A gap is present between the bottom surface of the overhanging posts and the culture chamber floor.

The valve mechanism was coupled to a mechanical actuation system through the pneumatic chamber layer. This layer is made of actuation chambers positioned directly underneath and in correspondence to the culture chambers. Upon application of a positive pressure to this layer, the assembly, constituted by the thin membrane and valve layer together as one, (*i.e.* the actuation membrane), bends upwards until it touches the bottom surface of the posts.

Two actuation chamber layouts were considered: separated actuation chambers (each 3900 μm × 1600 μm in dimension), one every other culture chamber (Fig. 1b), or a single common chamber for three culture chambers (12 300 μm × 1600 μm in dimension) (Fig. S1a†). A single inlet was present in both cases.

The device layout was realized so that three of the six chambers of the device were exposed to cyclic stretching while the other three lacked a corresponding actuation chamber underneath (thus serving as static controls). With the chosen layout, both a static and a dynamic triplicate could be achieved in the same device. A schematic representation of the device can be observed in Fig. 1b. while Fig. 1c depicts the sections of the device in the middle of a culture chamber (AA) and in between two adjacent chambers (BB). It is possible to notice how the actuation chamber is present exclusively underneath the culture chambers, not in

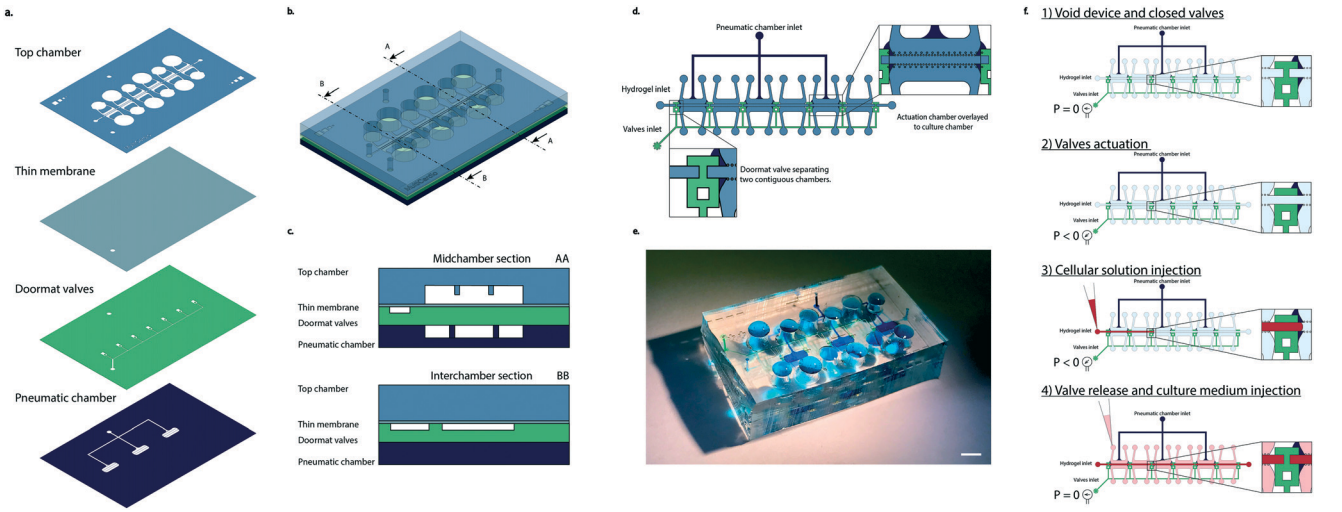

Fig. 1 Device layout. a. Device layers. PDMS structures are filled with colors while inner channels and apertures are left transparent. b. Device schematization. A mid-chamber section and an intra-chamber section are indicated with AA and BB, respectively. c. Schematization of two sections of the device. d. Device view from the top. Zoom ins (inset) on the intersection of separating walls and valves and on actuation chambers are highlighted. e. Example of the realized device. The different features were filled with colored dye to make them more visible. Culture chambers are highlighted in light blue, doormat valves in green, and pneumatic chambers in blue. The same color code of the schemes was maintained. Scale bar 4 mm. f. Device seeding operation schematics. 1) The device is initially empty and the closed valves separate the chambers from each other. 2) Applying a negative pressure to the valves' inlet causes the valves to open, putting the chambers in connection with each other. 3) While the negative pressure is still being applied to the device, the cellular solution (depicted in red) is injected into the chambers through a normal micropipette. From the zoom in it is visible how the advancing front of the cellular solution crosses from one chamber to the other. The two rows of posts flanking the central channel confine the cellular solution within the appropriate space. 4) The valve pressure is released, bringing it back to the atmospheric value. This causes the valves to close, separating the different compartments, as highlighted from the zoom in where it is visible how the cellular solution represented in red is divided by the valve (in green). Once the pressure has been released and the hydrogel containing cells has finished crosslinking, it is possible to inject the culture medium into the lateral channels and start the cyclic mechanical stimulation.

between adjacent ones where it could hinder proper closing of the doormat-like valves. Details of the device structure from a top view can be observed in Fig. 1d where the configuration with separated actuation chambers is depicted. Both valve and actuation layers have a single inlet (Fig. 1d and e). A schematic of the seeding procedure is depicted in Fig. 1f.

Device validation

Functional validation. The proper functioning of the device was evaluated according to the design specifications. A negative pressure is needed to open the doormat-like valves. A value of −0.5 bar was found to be necessary to obtain full valve opening, concurring with previous investigations.[28] Regarding the mechanical actuation pressure, a calibration curve was performed instead, with a previously introduced methodology,[20,22] to assess the minimal pressure sufficient to obtain contact between the bottom surface of the posts and the thin membrane. When the culture chambers are filled with coloured dye and different pressures are applied to the pneumatic chambers the colour intensity of the posts changes (Fig. 2a), this being a result of the different quantity of liquid present underneath the posts as the thin membrane moves towards them. The measured normalized mean grey intensity of the posts upon application of increasing pressures in different chips (for each chip all the three chambers were analysed, and the results averaged) is depicted in Fig. 2b. The optimal actuation pressure, defined as the onset of the plateau in the curves, was set at 0.8 bar (as highlighted by the red line in Fig. 2b) and adopted in the following experiments. While variability among devices was noticed, different chambers in the same device resulted in higher homogeneity in terms of actuation pressure. Fig. 2c depicts the variance of the mean grey intensity calculated among different devices (inter-chip variability) or among the three actuated chambers of a single device. It can be noticed how the chamber-to-chamber variability was significantly lower than the inter-chip variability.

By incorporating more chambers into a single device, therefore, it is feasible to further improve the control over the homogeneity of the applied mechanical stimulation. In our mechanical actuation system the stretching of cardiac constructs is achieved by increasing the pressure in the pneumatic chambers. This leads the membrane constituted by the PDMS layers in between the pneumatic chamber and the culture chamber to bend upwards until it reaches the bottom surface of the overhanging posts. The final stroke depends, therefore, solely on the gap present underneath the posts during the resting state.

To ensure the proper functioning of the device in generating independent constructs it is crucial that the doormat-like valves remain closed, despite the deflection caused by the cyclic mechanical activation. To verify this requirement, we tested the sealing of the valves during 7 days of cyclical stimulation. Two configurations of the actuation layer were taken into consideration: three separate actuations positioned in correspondence to every other culture chamber

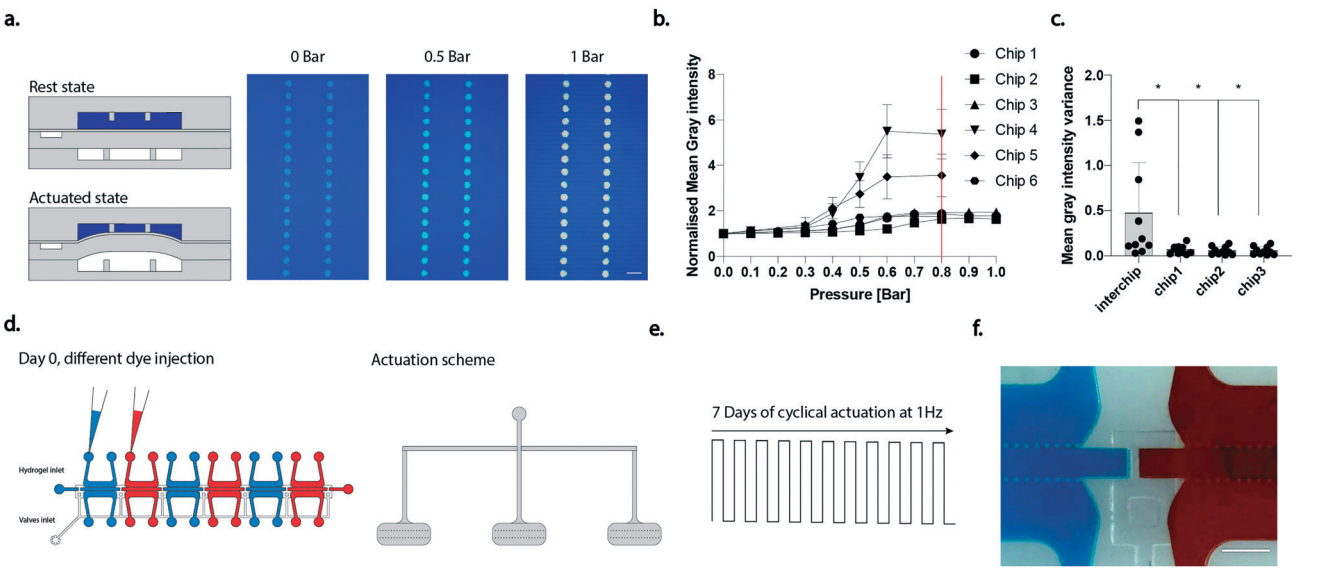

Fig. 2 Device functional validation. a. Schematization of the device in rest and actuated states upon filling of the culture chambers with blue dye and top views of the chamber when different pressures were applied. Scale bar 100 μm. b. Mean grey intensity of regions of interest within post areas against pressure applied in the actuation chamber. Results are presented as the mean in the three chambers for every device. Six different devices were considered. c. Variance of the mean grey intensity calculated among different devices or among different chambers of the same device. Each dot represents the variance of the mean grey intensity at a given pressure $*p < 0.05$, $**p < 0.01$. Statistics by one-way ANOVA with Dunnett's *post hoc* test. Three different devices were considered to have an immediate comparison with the three chambers of a single device. d. Schematization of the coloration of the chambers used to assess chamber independency. e. Scheme of the stimulation applied for 7 days. f. Device picture after 7 days of stimulation. Color diversity evidences the chamber separation. Scale bar 500 μm.

(Fig. 2d), and a single actuation covering three culture chambers, as visible in ESI† Fig. S1a. The top culture chambers were filled with coloured food dyes in alternating different colours (blue and red in Fig. 2d) and a cyclic stimulation (1 Hz) was applied for 7 days (Fig. 2e and S1b†). The separate actuation configuration allowed the chambers to be maintained independent even in the presence of mechanical stimulation, as evidenced by the maintenance of colour segregation in adjacent compartments (Fig. 2f). Conversely, the single actuation configuration was not efficient and, after 7 days, led to diffusion of the coloured dyes between adjacent chambers, demonstrating their fluidic connection (Fig. S1c†). The separate actuation configuration was therefore adopted in the following experiments. An alternative version of the device was also realized by increasing the distance in-between consecutive chambers, allowing for an actuation chamber to be positioned underneath each culture chamber, thus increasing the throughput of the stimulated constructs (Fig. S1d†).

Lastly, the stretch level experienced by the 3D cell micro-construct in the central channel was evaluated through the tracking of pairs of polystyrene beads embedded in fibrin gel. A mean stretching strain value of 8.5% was achieved (Fig. S2†).

Biological validation. A proof-of-concept of the newly proposed multi-chamber design functioning was performed comparing statically and mechanically stimulated constructs belonging to the same device. Previously published results, which were obtained in single chamber devices, were confirmed. Cardiac engineered tissues were generated with a mixed population of 80% CMs and 20% FBs.[12] Cells were injected into devices and cultured either under cyclic loading (8.5% of strain at a frequency of 1 Hz) or under static conditions. A custom made setup (Fig. S3†) was adopted to deliver an external electrical pace to constructs at the end of the culture period.

Brightfield images of the constructs after 5 days of culture are visible in Fig. S4a.† No tissue compaction was observed over time. The constructs, either in a static condition or under a cyclic loading, completely filled the central culture chamber at the end of the 5 days of culture (Fig. S4†). Only mechanically stimulated constructs responded homogeneously to the external electrical pace (Fig. S4b†),[16] showing a higher functionality and contraction ability compared to statically generated constructs. No differences were however visible in the overall cell morphology (Fig. S4c†).

A further biological validation was performed replicating, in the multi chamber device, results previously obtained in a single chamber *in vitro* scar model constituted by a population of 100% FBs.[12] FBs increased the expression of α-SMA (typical for the phenotypic FB switch to myofibroblasts) upon exposure for 5 days to either a biochemical cue (TGF-β1 supplementation) or to mechanical stimulation (10% strain at a frequency of 1 Hz) (Fig. S4d†) as previously reported.[12]

Assessment of co-culture population percentages

The effective distribution of the initial population obtained after cell isolation, nominally 80% CMs–20% FBs, was assessed through immunofluorescence at day 0, both in monolayer and 3D micro-construct cultures (Fig. S5†). Population ratios in 2D cell culture at day 0 were found to be 80.3% ± 2.99% CMs and 19.7% ± 2.99% FBs, while the percentages were found to be 82.1% ± 17.8% CMs and 17.9 ± 155.92% FBs in 3D microchambers (Fig. 3a). Quantifications of CMs and FBs showed similar values in 2D and 3D systems; no statistical differences with respect to populations nominal values were detected (Fig. 3a).

CMs and FBs distributions in 3D micro-constructs were also assessed after 5 days of culture under cyclic stimulation and considering different nominal population ratios in co-culture. Representative images are reported in Fig. S5.† The four experimental groups investigated consisted nominally of 80% CMs and 20% FBs (*i.e.*, high-CMs), 50% CMs and 50% FBs (*i.e.*, medium-CMs), 20% CMs and 80% FBs (*i.e.*, low-

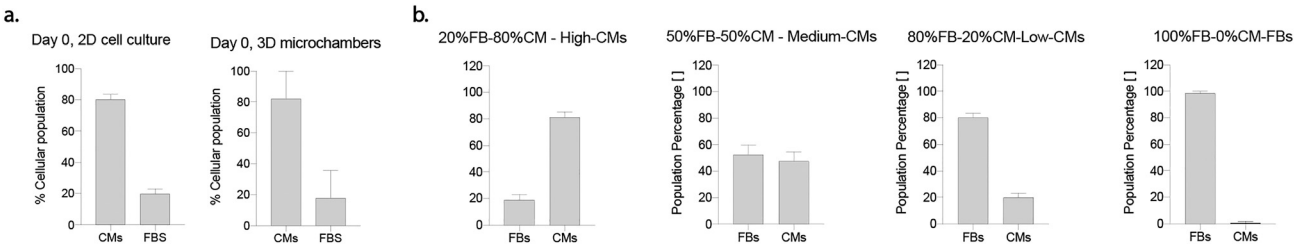

Fig. 3 a. Percentage of FBs and CMs in 2D and 3D culture systems. In both cases, no statistical significance was found with the nominal values of 80% CM and 20% FBs, respectively. n = 5 images belonging to N = 3 biologically independent samples were used for 3D quantifications and n = 6 images belonging to N = 3 biologically independent samples were used for 2D quantifications. A preliminary assessment where the considered populations were composed of either CMs or FBs was made (Fig. S5a†). At day 0, vimentin positivity was used to distinguish between cellular populations. Vimentin positive cells were considered to be FBs, and vimentin negative cells to be CMs (Fig. S5b†). b. Quantification of population percentages at day 5. Percentages of CMs and FBs were quantified after 5 days of culture and compared to the expected nominal values of the cocultures indicated in the graphs' titles. At least n = 5 images belonging to N = 3 biologically independent samples were considered in quantifications. At day 5, cTROP expressing cells were considered as CMs, and cells negative for cTROP were considered as FBs (Fig. S5c†). One sample t-test or Wilcoxon signed rank test were adopted to assess differences between a sample population, Gaussian or not respectively, and a theorical value. Statistical significance was indicated by $*p < 0.05$, $**p < 0.01$, $***p < 0.001$ and $****p < 0.0001$.

CMs), and 100% FBs (*i.e.*, FBs). The assessed CM and FB percentages did not exhibit any statistically significant difference with respect to nominal population values (Fig. 3b). The cell density of the different experimental

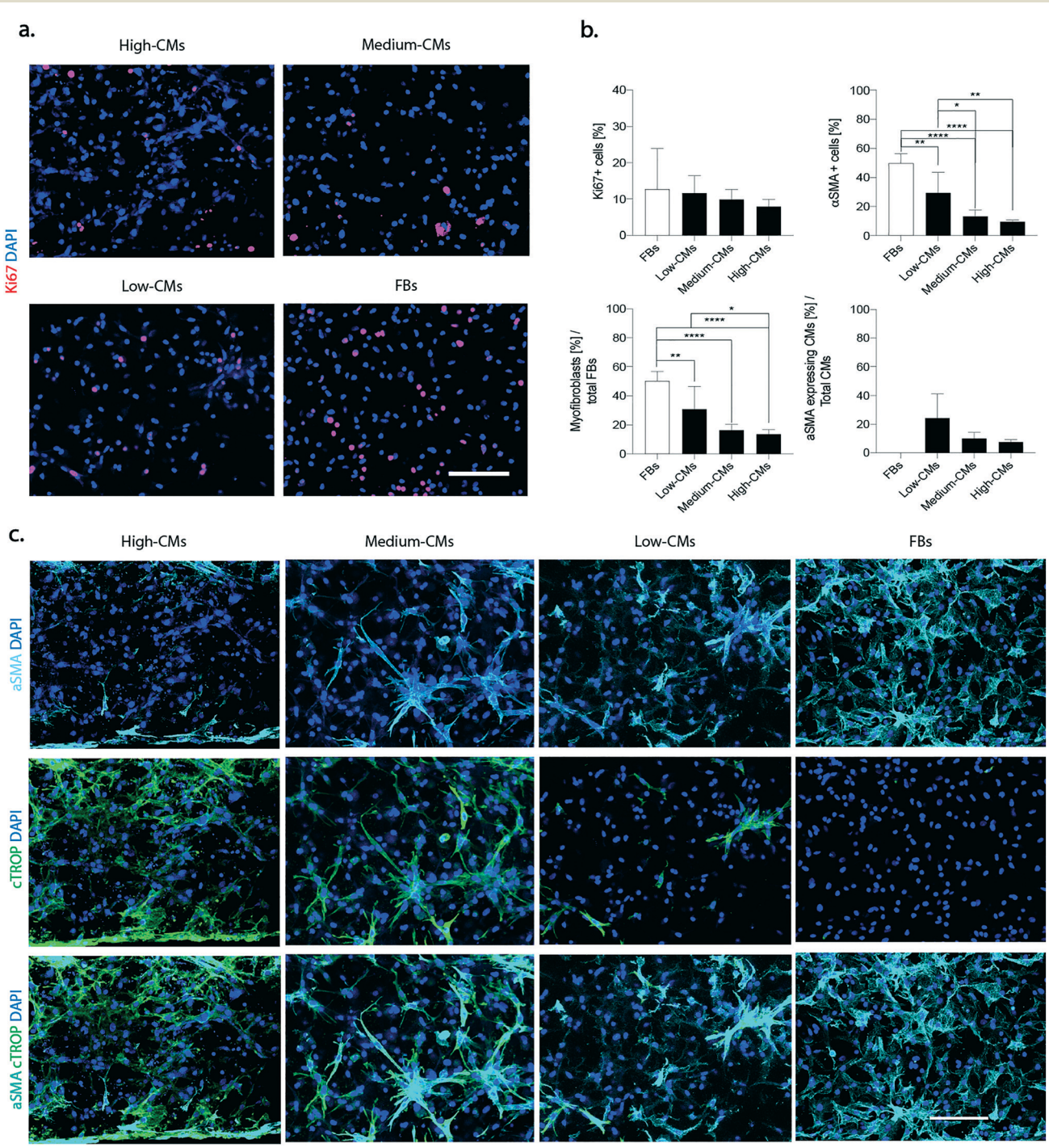

Fig. 4 Onset of fibrotic phenotype. a. Representative immunofluorescence pictures of Ki67 (red). Nuclei were stained with DAPI (blue). Scale bars 100 μm. b. Quantification of total proliferating cells: quantification of αSMA positive cells over the total cellular population, quantification of myofibroblasts over the total fibroblast population and quantification of hypertrophic cardiomyocytes over the total number of cardiomyocytes. At least $n = 5$ images belonging to $N = 3$ biologically independent samples for each condition were used for quantifications. The percentage of αSMA positive cells was determined as the number of cells expressing αSMA over the total number of cells. CMs were defined as cTROP+ cells; αSMA expressing CMs as cTROP+– αSMA+ cells; myofibroblasts were defined as cTROP–αSMA+ cells; FBs were defined as cTROP–αSMA-cells. Statistics by one-way ANOVA with Tukey's *post hoc* test for Gaussian populations and Kruskal–Wallis test with Dunn's *post hoc* test for non-Gaussian populations. *$p < 0.05$, **$p < 0.01$, ***$p < 0.001$ and ****$p < 0.0001$. c. Representative images of α-SMA (cyan) and cardiac troponin I (green) (c) of the four considered conditions after 5 days of culture under dynamic conditions. Nuclei were stained with DAPI (blue). Scale bars 100 μm.

groups after 5 days of 3D culture was also found to be similar ($p > 0.05$, Fig. S6†).

Effects of mechanical stimulation and different cardiomyocyte concentrations on cell proliferation and phenotype switch

The mitigating effects of different CM ratios on some of the early key steps of the wound healing cascade that follows myocardial infarction, namely FB proliferation[2] and FB phenotype switch into myofibroblasts,[31] were investigated at first. All the constructs were cultured under cyclical loading (1 Hz) for 5 days.

Proliferating cells, defined as Ki67-positive cells, were uniformly distributed throughout the constructs in all conditions (Fig. 4a), and their percentage decreased with the increase of the number of CMs (12.7 ± 11.2% in the FB condition, and 11.6 ± 4.7%, 9.8 ± 2.8%, and 7.8 ± 2.0% in the low-, medium- and high-CM population, respectively) ($p > 0.05$, Fig. 4b).

A distinction between Ki67 positive CMs and FBs was performed. Representative images are reported in Fig. S7a.† A slightly diminished percentage in Ki67 positive FBs over the total number of FBs was registered in the high-CM condition (Fig. S7b†) but, overall, the presence of an increasing number of CMs did not modulate the proliferative capacity of FBs with a clear trend. Extremely low numbers of Ki67 positive CMs were, instead, registered in all conditions (Fig. S7b†).

Immunofluorescence staining for the myofibroblast differentiation marker α-SMA showed a generally increased number of α-SMA positive cells with the decrease in the number of CMs in culture (Fig. 4c and S8†).

On top of being an indicator of switch to myofibroblasts, α-SMA is also expressed by hypertrophic CMs under diseased conditions,[32] even though it might also be a marker of less mature CMs during *in vitro* culture. Indeed, neonatal rat CMs were reported to be prone to a temporary re-arrangement and dedifferentiation of the contractile apparatus leading to a superior expression of alpha SMA instead of typical cardiac actin isoforms in *in vitro* culture.[33]

The typical "spread myofibroblast" morphology, as well as an increased number of α-SMA positive stress fibres was more evident in the 100% FB and in the low-CM conditions. Quantification of the total percentage of αSMA-positive cells confirmed that the highest number of αSMA-positive cells was present in the 100% FB condition (49.8% ± 6.4%) and was statistically different when compared to all other conditions (9.4% ± 1.1%, 13.2% ± 4.5%, and 29.3% ± 14.2% in the high-, medium- and low-CM condition, respectively) (Fig. 4b). A statistical difference was moreover detected between the low-CM condition with respect to both the high-CM and medium-CM conditions.

The percentage of myofibroblasts (*i.e.* the number of αSMA-positive/cTROP-negative cells normalized for the total number of FBs negative for cTROP) was 50.3% ± 6.5% in the FB condition, while it was statistically significantly lower in the high-CM condition (13.6 ± 3.2%), in the medium-CM condition (16.3% ± 4%), and in the low-CM condition (30.9% ± 15.7%) (Fig. 4b). A statistically significant difference was also evident between the low-CM and the high-CM populations.

The percentage of αSMA expressing CMs (*i.e.* the number of αSMA-positive/cTROP-positive cells normalised for the total number of CMs positive for cTROP) did not show statistically significant differences. However, a clear downward trend corresponded to decreasing quantities of FBs in the co-culture (7.6 ± 1.6%, 10.1 ± 4.2%, and 24.4 ± 16.8% in the high-, medium- and low-CM condition, respectively).

Compared to the other conditions, in the high-CM condition, αSMA-positive CMs were present exclusively at the edges in correspondence with the pillars (Fig. 4b).

Effect of coculture on matrix deposition and remodelling processes

An excessive matrix deposition leading to the formation of a fibrotic tissue is one of the hallmarks of cardiac fibrosis.[2] The deposition of two of the main constituents of the interstitial extracellular matrix (ECM), namely type I collagen and fibronectin, was investigated in the engineered micro-constructs (Fig. 5a and b). An enhanced accumulation of both fibronectin and type I collagen was detectable in micro-constructs with higher FB percentages, in particular at the edges of the constructs in correspondence with the pillars. While fibronectin was present in all conditions and its deposition seemed to increase with the increase of FB ratio in the culture, type I collagen was mainly deposited in the low CM condition. Higher percentages of fibroblasts corresponded also to an increasing trend in the expression of *Col3a1*, *Col1a1*, *Fn* (fibronectin), *Mmp2* and *Tnc* at the mRNA level (Fig. S9†). When the mRNA levels were normalized to the expression of the 100% FB condition, a trend of decrease in the expression of *Fn*, *Col1a1* and *Col3a1* was observed with the increase of CM percentage. The fold change in expression of *Fn*, *Col1a1* and *Col3a1* was significantly higher in the low-CM condition compared to the high-CM culture condition (0.71 ± 0.14 *vs.* 0.22 ± 0.04, 0.99 ± 0.15 *vs.* 0.27 ± 0.07, and 0.66 ± 0.06 *vs.* 0.21 ± 0.06 for *Fn*, *Col1a1* and *Col3a1*, respectively) (Fig. 5b).

Another peculiarity of fibrosis is an altered balance between deposition and degradation of the extracellular matrix. To assess this hallmark in the developed model, samples were analysed for mRNA expression of metalloproteinases *Mmp2* and *Mmp9*. While no statistical differences among conditions were detectable in the expression of these genes (Fig. S9†), the fold change (with respect to the 100% FB condition) showed a statistically significant increase in *Mmp2* for the low-CM condition with respect to the high-CM one (Fig. 6). Notably, a statistically significant decreasing trend was also visible in the fold change of *TGF-β1*, a pro-fibrotic factor, and in that of tenascin-C (*TnC*), an extracellular matrix protein expressed in

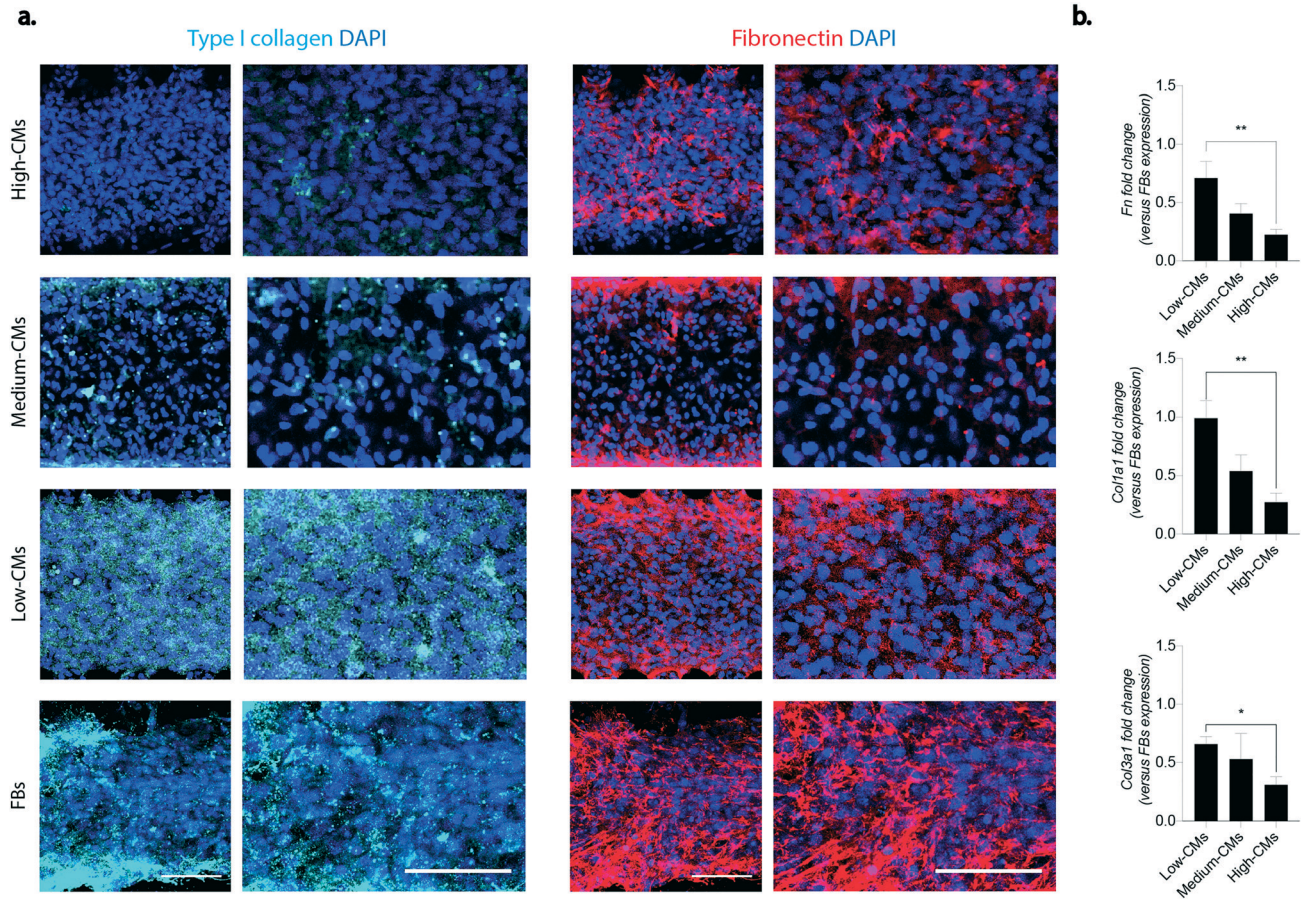

Fig. 5 Matrix deposition. a. Immunofluorescence of matrix components: type I collagen (in cyan) and fibronectin (in red). DAPI staining for nuclei is represented in blue. Images with a higher magnification are represented on the right of both columns. Scale bar 100 μm. At least four areas belonging to two biologically independent samples were considered. b. Relative gene expression of Col1a1, Col3a1 and fibronectin quantified by RT-qPCR. b-Actin was adopted as the housekeeping gene. Results were normalised to the FB population expression. *$p < 0.05$, **$p < 0.01$, ***$p < 0.001$ and ****$p < 0.0001$. Statistics by one-way ANOVA with Tukey's *post hoc* test for Gaussian populations and Kruskal–Wallis test with Dunn's *post hoc* test for non-Gaussian populations. At least $N = 4$ biologically independent samples were considered.

various diseases associated with inflammation and correlated with the onset of fibrosis in an *in vivo* pathological setting. While *TnC* expression is highly increased during embryonic development, it is suppressed in adult tissues. Upon injury or during remodelling, it is enhanced again, as well as in response to myofibroblasts under mechanical stretching. Meanwhile, *Nppa*, a factor known to contrast fibrosis which is usually upregulated under mechanical stretching,[34] was increased in the high-CM condition compared to the other culture ratios.

The expression of these genes was also evaluated in the starting populations, before seeding into the microfluidic devices (Fig. S10†). While *TnC* and *Nppa* at day 0 showed diminished but similar trends to those achieved after 5 days of cyclical stimulation (*i.e.* *TnC* diminished and *Nppa* increased with the percentage of CMs in culture), the decreased fold change which was visible for *TGF-β1* after stimulation was not observed at day 0. Moreover, *Mmp2* and *Mmp9* revealed opposite trends before and after the culture with the *Mmps* fold change increasing (and not diminishing) with the percentage of CMs in coculture.

Functional analysis

Only 3D engineered micro-constructs generated with either high- or medium-CMs were functional and followed the imposed external pacing. The Excitation Threshold (ET) was similar in the high- and medium-CM conditions (3.5 ± 1.7 V cm^{-1} and 3.6 ± 0.7 V cm^{-1}, respectively) (Fig. 7a). No statistical difference was found in the maximum capture rate (MCR) in the high- and medium-CM experimental groups (3.8 ± 1.5 Hz and 2.7 ± 1.0 Hz, respectively) (Fig. 7a).

Both conditions exhibited therefore synchronicity of cellular beating upon the application of an external electrical field. (ESI† Video 1). The variation of the position vector magnitude of the tracked cell during the contraction cycles (calculated as depicted in Fig. 7b) displayed synchronicity in contraction, with well synchronized contraction peaks and a contraction frequency coherent with the pacing (Fig. 7c). For each trajectory of contraction, the contraction direction (*i.e.*, the angle created between the direction and horizontal axis of the frame, Fig. 7d) was calculated. The probability density function (PDF) of the contraction direction was also

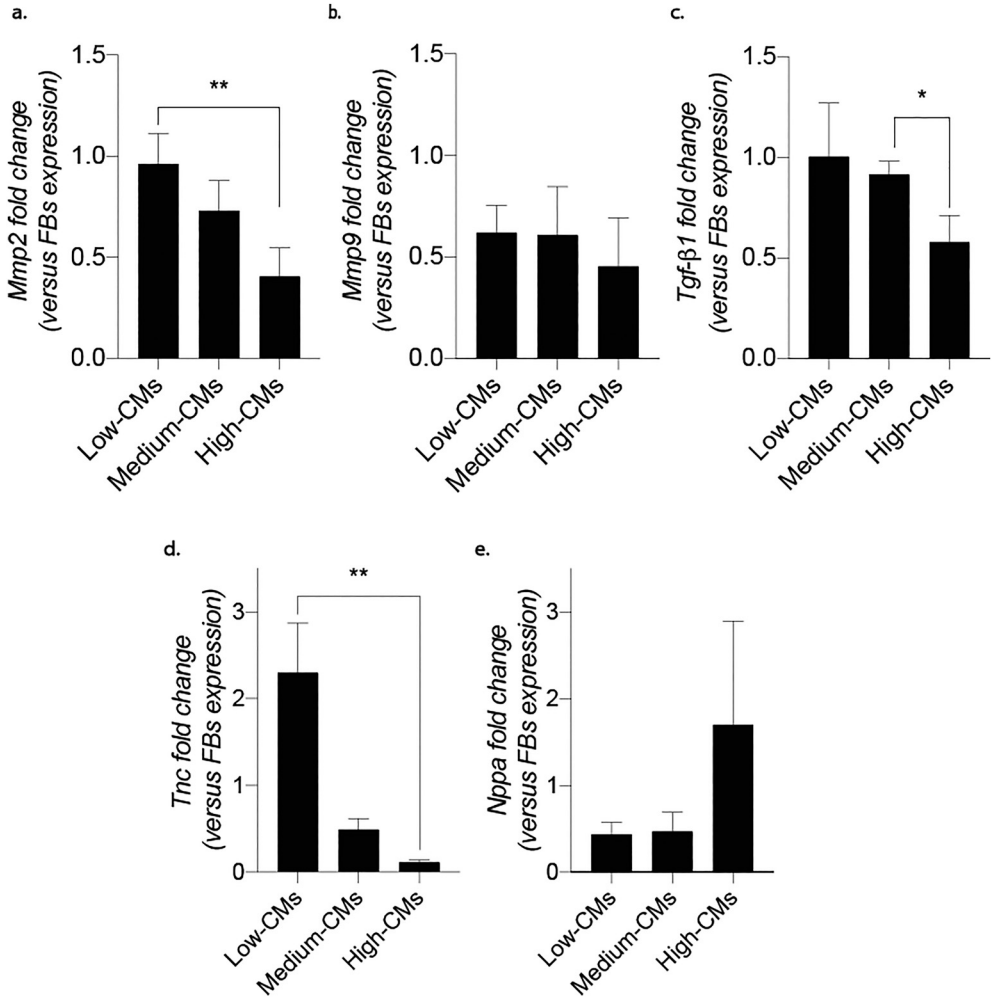

Fig. 6 Expression of factors involved in fibrosis modulation quantified by RT-qPCR. a and b. Expression of Mmp2 and Mmp9. c. Expression of TGF-β1. d. Expression of TnC. e. Expression of Nppa. b-Actin was adopted as the housekeeping gene. Results were normalised to the FBs population expression. $*p < 0.05$, $**p < 0.01$. Statistics by one-way ANOVA with Tukey's *post hoc* test for Gaussian populations and Kruskal–Wallis test with Dunn's *post hoc* test for non-Gaussian populations. At least $N = 4$ biologically independent samples were considered per condition.

estimated non-parametrically by a kernel smoothing estimation function in order to quantify and identify the most probable contraction direction within each ROI. In the high-CM group, the contraction direction was more aligned with the stimulation direction (namely 90°) compared to the medium-CM condition (Fig. 7e). The medium-CM group showed a higher probability (15.8 *vs.* 10%, in medium- and high-CM conditions, respectively) to find cells contracting perpendicularly to the stimulation direction (Fig. 7e).

Combination of mechanical stimulation and profibrotic factor TGF-β1

Mechanical stimulation alone induced neither an upregulation of pro-fibrotic markers, nor an increased myofibroblast phenotype switch in the high-CM condition (as previously shown[22]). The effect of the supplementation of a fibrosis trigger, namely TGF-β1, on top of mechanical loading, was also assessed. Evaluations were made exclusively in the high-CM condition, investigating the effect of the factor on physiological-like cellular ratios. Constructs obtained from high-CMs were exposed either to mechanical stimulation alone, namely TGFβ(−), or to mechanical stimulation and TGF-β1 (5 ng mL^{-1}), namely TGFβ(+), for 5 days (Fig. 8). CMs showed a similar morphology and density in both conditions and only a few cells were positive for αSMA (Fig. 8a). Few cells were positive for the proliferation marker (Ki67, Fig. 8a) and the number of proliferating cells seemed to increase following TGFβ-1 supplementation. Based on image analysis, a trend of increase was found when TGFβ-1 was supplemented; however no statistically significant differences were found between the two conditions for the percentage of proliferating cells (7.7% ± 1.8% and 12.5% ± 7.9% in TGFβ(−) and TGFβ(+), respectively) or of αSMA-positive (21.34 ± 7.25% and 29.9 ± 4.4% in TGFβ(−) and TGFβ(+) conditions, respectively) cells (Fig. 8b). Notably, both the number of hypertrophic CMs over the total number of CMs and of myofibroblasts over the total amount of FBs did

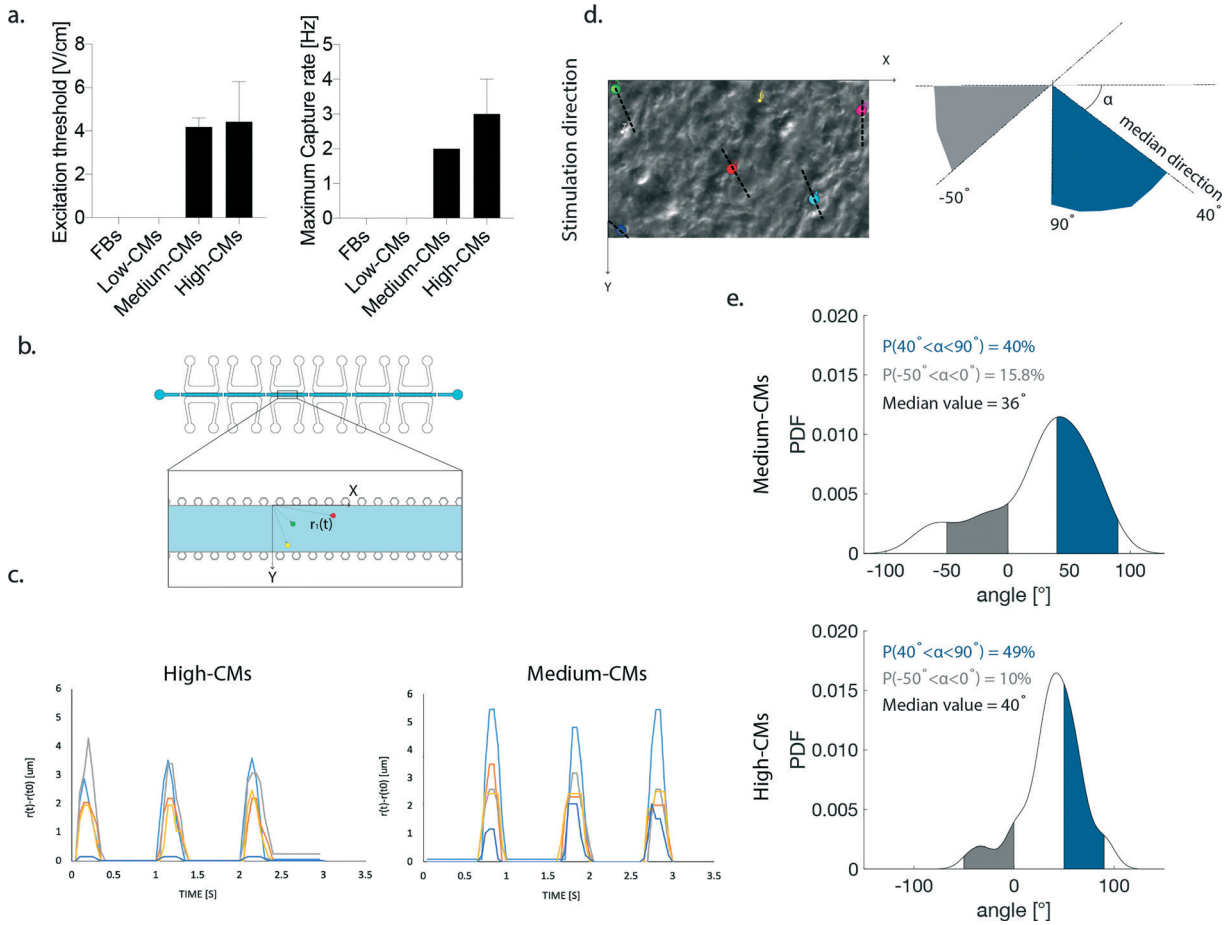

Fig. 7 Evaluation of contraction functionality of constructs. a. ET and MCR measured in the high and medium-CM conditions. Statistics by the Mann–Whitney test for non-Gaussian populations. ($p > 0.05$). b. Schematization of the coordinate reference system used in the assessment of beating synchronicity and contraction direction. Example position-vectors connecting the origin with three cells highlighted by coloured dots are displayed. c. Synchronicity of beating. Coloured lines represent the variation in the position vector modulus in time. Peaks corresponding to contraction demonstrate that cells beat synchronously in both conditions. d. Example of highlighted cells (coloured dots) used for the determination of the orientation angle. The direction along which each cell beats is highlighted by the dotted line. A schematization of the orientation along which cells contract is depicted on the right. e. Probability density function (PDF) of the contraction direction calculated for the high-CM and the medium CM conditions. Areas of alignment to the stimulation direction and opposite to it are highlighted in blue and grey, respectively.

not vary following TGFβ-1 supplementation. The levels of genes associated with fibrosis (*Col1a1*, *Col3a1* and *Fn*) and ECM degradation (*Mmp2* and *Mmp9*) were found comparable in the two conditions (Fig. 8c). A slight increase in the expression of *Col1a1* and *Col3a1* was detected in the TGFβ(+) condition. No statistical difference was anyway generally present between the two experimental conditions. The expression of *TGF-β1*, *Tnc* and *Nppa* also did not change between the two experimental conditions.

Discussion

In a proof-of-concept study recapitulating some of the hallmarks of cardiac fibrotic processes, we generated a new mid-throughput MPS including multiple independent samples within the same device and providing cyclic isotonic loading to 3D cardiac micro-constructs. Previous studies had addressed the incorporation of various types of mechanical stimulation in MPSs, mimicking the complex biological features[34] of constantly active organs and tissues (*e.g.*, lungs,[35] liver,[36] kidney[37] cartilage,[20] and heart[22]). However, MPSs capable of delivering mechanical loading were so far limited to single-chamber devices. Schneider *et al.*[38] were among the firsts to address the parallelization issue in a systematic way for cardiac-based models. The authors introduced a centrifuge-based system to generate parallel microconstructs allowing higher throughput and standardization. While this methodology was successful for CM-rich populations, their model wouldn't be able to directly apply a stretching mimicking the heart beating to FB-rich, fibrotic models, where synchronous beating does not happen spontaneously.

Building upon our previous experience,[28] we succeeded in coupling the functionalities of active mechanics and increased experimental yield by implementing a doormat-like valving system, which allows incorporation of multiple mechanically active, and biologically independent samples in the same device.

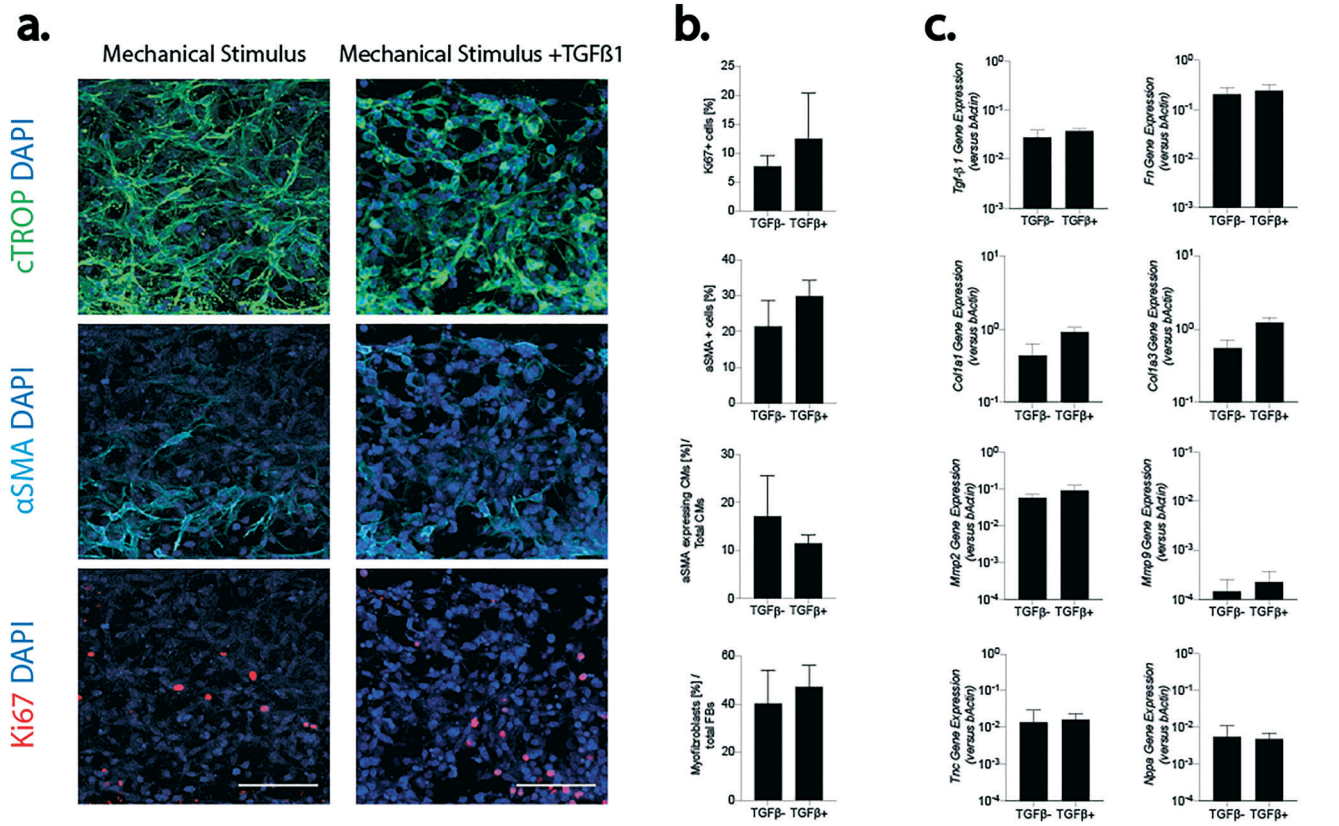

Fig. 8 The effect of the pro-fibrotic factor TGF-B1 on the high-CM microtissue control (80% CMs–20% FBs) was determined. a. Immunofluorescence staining of the two conditions for αSMA (cyan), cTROP (green), and Ki67 (red). DAPI marking nuclei is represented in blue. Scale bar 100 μm. b. Image quantifications. n = 6 representative areas belonging to N = 4 biologically independent samples were adopted in analyses. c. Quantification of representative genes made by RT-qPCR. At least N = 3 biologically independent samples were adopted in analyses. Comparisons were performed using two tailed t-test for Gaussian populations and Mann–Whitney test for non-Gaussian ones ($p > 0.05$).

Serially distributed, normally separated culture chambers could be thus connected during the injection of a 3D cell laden hydrogel and divided immediately afterwards. Moreover, properly tailoring the valve layer thickness made it possible to exploit it as an actuation membrane mobilised by pneumatic actuation chambers.

While the cyclical mechanical stimulation led to some leakage, impairing the samples' biological independence when the actuation and the valve were overlapped, this could be avoided by alternating static and dynamic chambers and/or by properly dimensioning the distance among them. Of note, the initial design was conceived to have, in a single device, both static and dynamically stimulated triplets of samples. This choice was made bearing in mind situations where a static control might be desired, like in models of musculoskeletal apparatuses.[20] The design could, however, easily be adapted so that all samples are subject to mechanical cues.

Additionally, including multiple chambers in a single device reduces the experimental variability usually occurring among different devices as well as the batch-to-batch variability, ultimately leading to more rigorous experimental conditions.

Markedly, the presented device allows an increased throughput without the need for perfusing the culture medium thanks to the PDMS gas permeability and the overall limited dimension of the central channel (300 μm in width). These features, as previously demonstrated,[22] allow indeed an optimal diffusion of oxygen and nutrients from the lateral culture medium channels.

A systematic review of the present MPS panorama in terms of throughput and experimental yield was recently proposed by Probst, Schneider, and Loskill,[39] highlighting how, so far, most MPSs are based on individual unit platforms. Exclusively a few attempts have been made at delivering multiple independent chambers, with devices incorporating from 12 to 96 well-like structures defined as high-throughput despite being still far from the yield necessary for big data to be made available from MPS-based experimental campaigns.

With the proposed device, therefore, introducing 6 independent chambers we are collocated in the mid-throughput range in terms of currently available MPSs. Still, as we previously demonstrated,[28] multiple chamber lines could easily be incorporated within the area of a 96 well plate, further increasing the overall throughput. Moreover, we are, as of our knowledge, among the firsts to render such a parallelization possible with a mechanically active device.

The proposed device was key in analysing the effects of different ratios of CMs and FBs in the assumption of some of the hallmarks of the wound healing cascade, within a 3D mechanically active environment, and without the supplementation of pro-fibrotic factors.

FB proliferation, together with FB migration, is one of the first cellular processes starting upon injury and it was already demonstrated to increase, upon either chemical or mechanical stimuli, in an *in vitro* MPS, with microconstructs composed of either only FBs[12] or 80% of CMs and 20% of FBs.[22] At day 5, the expression of Ki67 was not statistically different among conditions, but a slight decreasing trend was visible in the experimental groups with a lower number of FBs. Notably, the percentages measured in this work were in line with values previously detected[12] (around 10% of the total cell population), and no differences were detectable in the cellular density at the end of culture despite the lower density used to seed FBs alone.

Another salient tract of fibrosis is the expression of contractile stress fibres. Previous models based on MPSs and microfluidic devices highlighted the expression of αSMA in fibrotic constructs, even of human origin.[23] When cells were allowed to self-assemble, however, they resulted in constructs with high expression of stress fibres, possibly limiting the discerning capacity on the assumption of a hypertrophic phenotype; moreover αSMA expression was linked to CM dedifferentiation in *in vitro* cultures.[33] Usage of a soft fibrin hydrogel and of a tailored confining chamber design allowed minimal αSMA expression under physiological (*i.e.*, high CMs) conditions.

Cyclic mechanical stimulation alone induced a profibrotic phenotype in FBs and CMs with both cell types expressing the contractile protein αSMA. This points to the fact that a physiological stretching level (*i.e.*, 8.5%) might be sufficient for a pathological remodelling with altered non-physiological population ratios. Remarkably, the total percentage of αSMA expressing cells decreased with respect to the FB condition used as a positive control,[12] even with just 20% CMs present in co-culture. The same fact was observed for both the percentage of CMs and FBs expressing hypertrophic features, suggesting a dampening effect of CMs on the profibrotic environment and modulation of FB behaviour through a probable cross talk.

In vivo intracellular communications within the myocardium are mediated by a complex interplay of electrical and mechanical messages together with biochemical factors (*e.g.* paracrine factors and microRNAs).[40] While our findings revealed how fibrotic traits could be modulated by different percentages of FBs in the presence of only a physiological cyclic stimulation, further mechanistic oriented studies should be conducted to uncover the mechanisms behind the observed effects.

In the presented co-culture model, we also observed the increased deposition of ECM proteins, which is typical of scar formation. The increase in type I collagen and fibronectin, detected both at the gene level and through immunofluorescence, revealed higher matrix deposition in FB-rich co-cultures. With respect to previously published stiff-hydrogel-based fibrotic models where collagen was mainly intracellular,[1] a homogeneous protein distribution could be detected in our micro-constructs. This observation pointed towards the beneficial effect of introducing cyclical stretching, while allowing ECM deposition to increase when using soft hydrogels and higher CM percentages.

Matrix turnover was also increased as indicated by the expression of the degrading metalloproteinases *Mmp2* (but not of *Mmp9*). Numerous *in vivo* and *in vitro* studies revealed the involvement of the gelatinases Mmp2 and Mmp9 in the altered ECM homeostasis typical of fibrosis.

Evidence showed that MMP9, together with MMP8 and MMP12,[41] is however, linked to the presence of infiltrating neutrophils and macrophages, not presented in this study.

The fact that *Mmp2* expression positively correlated with the percentage of CMs before the culture and negatively after, together with the modulation of *TGF-β1*, visible exclusively after 3D co-culture and stimulation, further supports the validity of the presented model in inducing fibrosis hallmarks.

Furthermore, an analysis of two possible indicators of cross-talks between FBs and CMs was performed. TnC is an extracellular protein[42] expressed during heart development and suppressed in adult tissues. Its expression is activated again upon injury or remodelling, and in response to mechanical strain in FBs.[43,44] In our results, TnC expression decreased with decreasing number of FBs. The NppA gene correlates with inflammation/degradation and ECM promotion. A slight increase in the expression of NppA was detected in the high-CM population as expected given the enhanced expression by CMs.[16] These trends were visible also in the initial populations, although with lower modulations. Further enquiries should therefore be conducted in order to be able to ascribe the observed modulations to a particular phenomenon or cellular population.

Indeed, a model considering different FB concentrations allowed for an in-depth study of different stages of deterioration and could possibly give us insights on the effect of pharmacological treatments as well as on the functional properties at different pathological levels.

On this last matter the assessment of cardiac functionality revealed that the constructs engineered with a low number of CMs did not synchronously follow the external electrical stimulation. This lack might be indicative of the representativeness of our model of an advanced fibrotic state, in which the combined effects of the low number of CMs, increased ECM deposition, and presence of myofibroblasts might impair the electrical signal propagation. Medium-CM constructs could beat synchronously confirming previous findings, demonstrating the presence of a 50% cardiac fibroblast threshold, above which the contractility properties of the engineered cardiac constructs are severely compromised.[17]

Notably, the custom-made electrical setup adopted in the present work for the functional assessment (Fig. S3†) shows a

limited contact between the conductive culture medium and the electrodes, thus probably resulting in a low local field within the constructs. To overcome this issue, electrode guides bringing them in direct proximity of the cultured constructs might be introduced in the device as recently published.[45]

Finally, we also tested the resistance of the high-CM population to fibrosis induction when both cyclical stretching was provided, and the profibrotic factor TGF-β1 was administered. Both immunofluorescence and RT-qPCR revealed that the high-CM condition seemed to resist the onset of a fibrotic phenotype with only a slight increase in fibrosis associated gene expression.

Mastikhina *et al.*[23] managed to recapitulate the different key features of fibrosis by co-culturing human iPSC-CMs and cardiac FBs (at a ratio of 3 : 1) in a novel MPS using passive tension and TGF-β1 as a fibrotic trigger. In our co-culture model of neonatal rat CMs and FBs in the high-CM condition (80% CMs–20% FBs corresponding to a ratio of 4 : 1) none of the investigated traits of fibrosis was upregulated, even under an active cyclic stimulation and with the additional supplementation of TGF-β1. In our experimental set-up, human recombinant TGF-β1 was used on cells of rat origin. Nevertheless, the human recombinant morphogenic molecule is known to share 99% amino acid identity with rat TGF-β1. Moreover, human recombinant TGF-β1 was previously successfully used to trigger fibrotic traits in constructs generated by only cardiac rat FBs (Fig. S 4d†).[12]

The different outcome obtained in ref. 23 with respect to our study might, therefore, be explained by the use of a different cell origin (human instead of rat), different adopted culture times (14 days instead of 5), the higher concentration of human recombinant TGF β1 used in ref. 23 together with its use to pre-activated FBs in monolayer culture, and the different mechanical stimulation and 3D environment.

A superior fibrosis stimulus, such as higher TGF-β1 concentration or FB pre-activation in monolayer culture, might hence be needed to induce fibrosis traits with a high CM density in the present setup. Further enquiries should therefore be conducted in this regard, possibly combining TGF-β1 and mechanical stimulation and providing not physiological (*i.e.* 8.5% like in our case) but pathological deformation (*e.g.* with a strain level superior to 15% (ref. 13)).

Summing up, therefore we successfully engineered a mid-throughput, mechanically active MPS device providing a useful tool to reproduce, through a co-culture model, some fibrosis traits *in vitro*.

Nevertheless, there are some limitations in the presented study and on the MPS platform that are worthy of further discussion.

Firstly, an in-depth investigation of the interplays between CMs and FBs would require separate analyses of the two populations after culture. Performing cell sorting and gene expression analysis on different cell subpopulations is, however, highly technically demanding in microfluidic devices. Moreover, while limiting the construct dimension does increase the number of replicates per experiment and the operational ease, it also further lowers the number of cells per construct. *In vitro* models with a higher cellular yield or more sophisticated analysis methods (*e.g.* single cell RNA) might, therefore, be needed to address mechanistic questions.

Nevertheless, in the presence of a fibrotic stimulus CMs were also reported to start expressing the typical markers of fibrosis, such as *Col1a1*, TnC and metalloproteinases,[46] making the results here presented of general interest.

Secondly, a certain variability in cell spatial distribution and population ratios was noticeable within different areas of the same experimental group. A defined level of inhomogeneity in the cellular populations is the natural result of the mixing and injection processes together with the limited scale adopted in the present device. Images in Fig. S8† were specifically included to highlight this possible limitation, which was particularly evident in the condition with 50% FBs and 50% CMs. The use of a hydrogel with a slower polymerization rate than the fibrin gel composition here adopted, allowing for the preparation of bigger cellular solution aliquots, might help in increasing the homogeneity of the cell spatial distribution.

Despite these shortcomings, we presented an innovative mid-throughput and mechanically active device and our findings highlighted the relevance of the choice of a suitable FB and CM ratio, and the possible effects of the mechanical loading (even when applied in a physiological range) when aiming at mimicking cardiac fibrosis hallmarks *in vitro*.

Moreover, the here investigated different CM and FB co-culture ratios could also be representative of either the time evolution of fibrosis or of different areas of the damaged myocardium (scar region, border zone, not damaged area) upon a myocardial infarction.

Conclusions

We introduced a new MPS coupling a mechanically active environment with a higher throughput and we successfully exploited it to study how different percentages of CMs and FBs affect the possible onset of a fibrotic phenotype. The different ratios of CMs and FBs could be used to mimic different steps of the pathology and/or different regions of the affected myocardium (*e.g.* the scar tissue, or the border zone with still few living CMs). Therefore, such a model could help in better understanding the development of the pathology and in possibly envisioning new anti-fibrotic therapeutic solutions. Moreover, the proposed design could be generalised and adapted to provide, for instance, compression rather than stretching, making it useful in modelling musculoskeletal pathologies. We presented therefore a possible valuable instrument for both disease research and drug development and screening campaigns.

Materials and methods

Device design and fabrication

Layers constituting the device, namely the top culture chamber, thin un-patterned membrane, doormat valve layer, and pneumatic chamber layer (Fig. 1a), were fabricated through soft-lithography of PDMS (Sylgard 184, Dow Corning) onto SU-8 master molds (Microchem).

The top chamber is constituted by six different culture chambers in series, separated from each other by 200 μm wide PDMS walls. Each of the culture chambers is composed of a central channel (300 μm wide) separated by two rows of hexagonal overhanging posts (28 μm side, 50 μm apart from each other) from lateral medium channels. A gap is present between the posts and the layer underneath. Post and gap heights (100 μm and 50 μm, respectively) were designed so that a defined lateral expansion of the constructs could be achieved (*i.e.* 10%).[22]

The valves, conceived in the fashion of normally closed doormat-like valves,[30] are constituted by interconnected rectangular shaped cavities (1200 μm × 700 μm × 150 μm) closed by the thin membrane (100 μm in thickness) and positioned underneath the walls separating the culture chambers. A squared post (300 μm × 300 μm) is present in the middle of the valves to prevent the thin layer from collapsing under normal pressure conditions. Each actuation chamber is equipped with two rows of round posts (diameter 50 μm and set 200 μm apart) to prevent sagging.

The device's layouts were designed through Autocad (Autodesk) and the corresponding photomasks printed at high resolution (64 000 DPI) on polyester transparent films (JD Photodata). The layers' master molds were obtained through photolithography. Multilayer photolithography was employed for the fabrication of the culture layer. Briefly, a gap layer (height 50 μm) and a post layer (height 100 μm) were subsequently realized with SU-8 photoresist (Microchem) onto a 4-inch silicon wafer substrate carefully aligning and creating the appropriate features through a mask aligner (Karl-Süss MA6/MA8 mask aligner).

Classic photolithography was employed for the generation of doormat valve (height 150 μm) and pneumatic chamber layers (height 150 μm). Master-molds were realized in a clean room facility (Polifab, Politecnico di Milano, Milano).

Layers were realized in polydimethylsiloxane by mixing the PDMS base and curing agent at a 10 : 1 w/w ratio, and allowing polymerization on master-molds at 65 °C for at least 2 hours.

Thin membranes, which are un-patterned PDMS layers, were realized by pouring PDMS on a smooth, 4 inch, silicon wafer. A 100 μm thickness was obtained through spin coating (800 rpm, 60 s).

The valve layer's overall thickness (900 μm) was controlled by pouring defined quantities of PDMS onto the valve layer master mold.

PDMS stamps were peeled off the molds and appropriate holes were bored at the various inlets (1 mm diameter for the actuation chamber, 0.5 mm diameter for the valve layer, 0.5 mm for the pneumatic chamber layer, and 3 or 4 mm for the media reservoirs in the culture chambers). Surfaces to be bonded together were treated with air plasma (Harrick Plasma Inc.) and brought into contact after careful manual alignment. Bonded layers were left at 65 °C for at least 30 minutes after bonding. The doormat valve layer was bonded directly onto the thin membrane coated 4 inch wafer. Bonding of the valve layer before peeling off the membrane eased the detachment without tearing of the membrane. During bonding between the culture chamber and the valve-thin membrane layer assembly, a negative pressure was applied to the valve layer. This procedure prevented permanent bonding of the thin membrane to the bottom surface of the PDMS walls which separate the different culture chambers, thus prejudicing the device's working principle. Devices were bagged and sterilized through autoclaving before use.

Device functional validation

Both the negative pressure necessary for valve opening during injection and the positive pressure necessary for device actuation were characterized as previously described.[22,28] The negative pressure required to obtain full opening of the valve depends on the thickness of the thin membrane. A fixed thickness of 100 μm was adopted, as previously optimized by Visone *et al.*,[28] to ensure valve movement with a negative pressure of −0.5 bar. Confirmation of the full aperture of the valves at the chosen pressure was carried out as previously described[28] (data not shown).

The valve layer thickness was optimized so that the cumulative thickness of the thin membrane (100 μm) and valve layer (900 μm), constituting together the actuation membrane, reached 1 mm. A calibration procedure was performed to determine the effective actuation pressure, defined as the pressure level needed to bring the top surface of the membrane into contact with the posts. Concisely, the entire top culture chamber was filled with a blue dye. Given the transparency of PDMS and the presence of the dye-filled gap underneath the posts, the posts themselves appear as blue in the rest condition (Fig. 2a). Upon contact between the posts and actuation membrane, no more dye is left in between the PDMS structures and posts appear as white. The grey mean intensity of the images taken at different pressures of the actuation chambers was measured as an indication of the distance between posts and actuation membrane, and the actuation pressure defined as the plateau present in the grey mean intensity *versus* pressure graph (Fig. 2b). Three regions of interest corresponding to three different posts were considered per each image. Three chambers per device, belonging to 6 different devices, were used in the measurement. The grey mean intensity levels were normalized for the value measured at atmospheric pressure. The standard deviation of the normalized mean grey intensity at the different pressure levels of three chambers belonging

to the same device or to three separate devices was used as an indicator of device uniformity.

Permanence of chamber separation upon application of a cyclic mechanical stimulation was tested. As mentioned, two designs were considered regarding the actuation layer: one in which a single actuation chamber covered the first three culture chambers, (Fig. 2d) and one in which three separate actuation chambers were associated with non-continuous culture chambers (Fig. S1†). The separation of adjacent culture chambers was tested in both cases. Culture chambers were filled with coloured dye (a different colour for adjacent chambers) in the closed valve configuration and devices were stimulated (0.6 atm, 1 Hz) for 7 days. Pictures of adjacent chambers were taken during the stimulation time.

The effective strain field applied to the constructs was also measured as previously described.[22] Briefly, polystyrene beads were embedded in the same fibrin gel later on used for cell culture and images were taken under different pressure conditions (Fig. S2†). The relative position of different couples of beads was used to determine the monoaxial stretching applied following the formula:

$$\varepsilon_{xx} = \frac{(\Delta x)_p - (\Delta x)_0}{(\Delta x)_0} = \frac{\left[(x_1)_p - (x_2)_p\right] - \left[(x_1)_0 - (x_2)_0\right]}{\left[(x_1)_0 - (x_2)_0\right]}$$

where $(\Delta x)_p$ is the distance projected along the x axis between two beads at a definite pressure level p, and $(\Delta x)_0$ is the distance projected along the x axis between two beads at atmospheric pressure. Four couples of beads were considered for each chamber. Six different chambers belonging to two different devices were used in the quantification.

Cell harvesting and isolation

Neonatal rat cardiomyocytes (CMs) and fibroblasts (FBs) were isolated from 2–3 day old Sprague Dawley rat hearts as previously described.[47] Isolation was performed according to the Swiss Federal guidelines for animal welfare with procedures approved by the Veterinary Office of the Canton Basel (Basel, Switzerland). Rat ventricles were quartered, digested overnight in a 0.06% (w/v) solution of trypsin in Hank's balanced salt solution (HBSS, Gibco) followed by five digestion steps of 4 min each, at 37 °C and 150 rpm, in a 0.1% (w/v) type II collagenase (Worthington, Biochemical Corporation) solution. Isolated cells were pre-plated in growth medium (high glucose DMEM supplemented with 10% v/v foetal bovine serum (FBS, Hyclone), 1% v/v penicillin streptomycin, 1% glutamine, and 1% v/v HEPES) for 45 min to allow FB adhesion (all reagents purchased from Sigma Aldrich unless differently specified). Following the pre-plating, a 100 FB population was adherent to the flask and kept in culture, while a mixed cardiac cell population enriched with CMs (roughly 80% CMs and 20% FBs) was collected and separately cultured overnight (37 °C, 95% humidity and 5% CO_2) before starting the experiment.[22] FBs were used following either overnight incubation or frozen in liquid nitrogen and used later (up to passage p3).

3D cell culture in the microfluidic device

Four different co-culture ratios of CMs and FBs were considered: 20% FBs and 80% CMs (high-CMs), 50% CMs and 50% FBs (medium-CMs), 20% CMs and 80% FBs (low-CMs), and a population composed exclusively of FBs which was used as a control.[12] Medium and low CM experimental groups were obtained by diluting with FBs the initially isolated cardiac population enriched with CMs (80% CMs and 20% FBs).

CMs and FBs were detached using 0.25% trypsin/1 mM EDTA (Gibco), mixed at appropriate ratios, embedded in fibrin hydrogels (20 mg ml^{-1} of fibrinogen, 2.5 U ml^{-1} of thrombin, 2.24 TIU per mL of aprotinin, 20 mM of calcium chloride), and immediately injected into the micro devices. All co-culture populations were seeded at a density of 100×10^6 cells per ml. The control group of 100% FBs was prepared with a cell density of 14.5×10^6 cells per ml as previously established.[12]

Cell-based fibrin gels were simultaneously injected into the six chambers of the microfluidic device by applying a negative pressure to the valve layer that allowed the valves, normally closed, to open. Immediately after the injection of the cell laden fibrin solution, the pressure was released and microdevices were put in the incubator (at 37 °C, 95% humidity and 5% CO_2) for 10 minutes to complete the polymerization of the hydrogel before filling the side channels of the culture layer with growth medium. Constructs were cultured for additional 5 days in growth medium. Culture medium was changed every day by simply removing the exhaust medium from the reservoirs and adding a fresh one.

To reduce the fibrin gel degradation, aprotinin (Sigma-Aldrich) was supplemented during the first days of culture at a concentration of 1.15 TIU per mL on day 0 and at a decreasing amount in the following three days (80%, 60% and 40% of day 0 on day 1, 2 and 3, respectively).

Cyclic stimulation (1 Hz, 0.8 bar) was started immediately after polymerization and applied for the 5 days of culture. A custom-made controller[20] connected to a pressure regulator (Comhas) was used to provide devices with the mechanical stimulation.

3D micro-tissues generated by 80% CMs and 20% FBs cultured in growth medium with the daily supplementation of 5 ng mL^{-1} of human recombinant transforming growth factor-β1 (TGF-β1, Sigma-Aldrich) in addition to the mechanical stimulation were also considered.

To verify the ratio of CMs and FBs in the freshly isolated enriched CM cell population, both 3D micro-tissues and cell monolayers (125×10^3 cells per cm^2) on glass slides (Ted-Pella Inc., 10 mm diameter, 0.13–0.17 mm thickness) were prepared and stopped for analysis at day 0.

Immunofluorescence staining

Immunofluorescence was performed on both cells seeded on glass slides, at day 0, and on 3D whole micro-tissues, directly within the culture chamber (either at day 0 or after 5 days of culture). Samples were fixed in 4% paraformaldehyde (PFA) for 180 minutes at room temperature and incubated in a solution of 0.3% Triton X-100 (Sigma), 2% BSA, and 5% serum (donkey serum was used for 3D micro-tissues and cell monolayer stained at day 0, goat serum in all other samples) in phosphate-buffered saline (PBS, Gibco) for 45 minutes at room temperature in order to permeabilize cells and block nonspecific binding. Samples were then incubated overnight at 4 °C with the following primary antibodies: polyclonal rabbit anti-rat Ki67 (Ab15580, dilution 1 : 200), monoclonal IgG2a mouse anti-rat alpha-smooth muscle actin (α-SMA, A2547, dilution 1 : 400), monoclonal mouse IgG2b anti-rat cardiac troponin I (ab200080, dilution 1 : 100), polyclonal goat anti-rat vimentin (SC-7557, dilution 1 : 200), polyclonal mouse anti-rat collagen type I (NB60450, dilution 1 : 200), and polyclonal rabbit anti-rat fibronectin (Ab2413). Fluorescently labelled secondary antibodies (AlexaFluor) were used at a 1 : 200 dilution and incubated for 6 hours at 4 °C. 4′,6-Diamidino-2-phenylindole (DAPI) was used to stain nuclei.

Image analyses

All images were taken with a 20× objective on a fluorescence CLSM (Zeiss LSM 710 confocal microscope for quantification and Nikon AR 1 ALA for matrix staining and cell monolayer culture) and analysed by using Image J (NIH) software. All images of the 3D micro-tissues were acquired longitudinally and included the two rows of posts at the top and bottom so that the cell strain direction coincides with the top-bottom axis of the image. All image analyses were conducted in the regions of interest excluding areas near the posts, focusing on the effect of the cyclic strain and avoiding any confounding effect due to the passive tension of post adhering CMs.

Assessment of CM and FB ratio. The ratio of CM and FB populations was determined through immunofluorescence staining both at day 0 and at day 5. After a preliminary evaluation showing that cells were either CMs (*i.e.* cTROP positive) or FBs (*i.e.* vimentin positive), as highlighted in Fig. S5a,† quantifications were performed according to either cTROP or vimentin positivity. At day 0, freshly isolated cardiac cells were seeded in monolayer or used to generate 3D micro-tissues and immediately processed for immunofluorescence staining. Cell nuclei, stained with DAPI, were counted to quantify the total number of cells. FBs were defined as vimentin-positive cells, while CMs were defined as cells negative for the vimentin staining. At day 5, the ratio of CMs and FBs in the population was evaluated for all co-culture conditions. Cell nuclei, stained with DAPI, were counted to quantify the total number of cells. CMs were defined as cells positive for cTROP, FBs as negative ones. Percentages were calculated as the number of CMs and FBs over the total number of cells respectively. At least $n = 5$ images belonging to $N = 3$ biologically independent samples per condition were considered in quantifications.

Quantification of proliferating cells. The percentage of proliferating cells was assessed by quantifying Ki67 positive cells over the total number of cells. Percentages were calculated as the number of Ki67 positive cells over the total number of cells. At least $n = 5$ areas belonging to $N = 5$ biologically independent samples were considered in quantifications.

Quantification of αSMA-expressing cells. αSMA expressing CMs were defined as cardiac troponin I-positive and αSMA-positive cells, while myofibroblasts were defined as αSMA-positive and troponin I-negative cells. αSMA expressing CMs were not calculated in the FB only population.

The percentage of αSMA expressing CMs over the total amount of CMs was calculated as the number of cells positive for both αSMA and cTROP, over the number of cells positive for cTROP. The percentage of myofibroblasts over the total amount of FBs was calculated as the number of cells negative for cTROP and positive for αSMA over the number of cells negative for cTROP. At least $n = 5$ different images belonging to $N = 3$ biologically independent samples were used for quantifications. An overview of images used for quantifications is visible in Fig. S8.†

Quantitative RT-PCR

Micro-tissues were retrieved opening the microdevices and digested in TRI-Reagent (Sigma) and the total mRNA isolated adapting a previously described protocol.[48] An Ominiscript reverse transcription kit (Qiagen) was used for extracting cDNA from mRNA. Quantitative real-time PCR (qRT-PCR) was performed using TaqMan assays using an ABI 7300 TR-PCR system (Applied biosystem, Carlsbad). Expression of *Col1a1* (Rn01463848_m1), *Col3a1* (Rn01437681_m1), *Fn* (Rn00569575_m1), *Tnc* (Rn01454947_m1) *Mmp2* (Rn01538170_m1), *Mmp9* (Rn00579162_m1), *Tgfβ1* (Rn00572010_m1), and *Nppa* (Rn00561661_m1) was checked. *Actb* (Rn00588290_m1) was used as the housekeeping gene. At least three biologically independent samples were considered for each condition.

Analyses were repeated on cellular populations before the culture period; CMs and FBs were mixed according to the different specified ratios and digested in TRI-Reagent (Sigma). Three samples for each condition were considered.

Contractile functionality assessment

The functional beating capability of the 3D micro-tissues under different conditions was assessed after 5 days of culture. Electrical pacing was imposed using two carbon rod electrodes, put in contact with the medium reservoirs, and aligned with the longitudinal direction of the chambers, symmetrical with respect to the central axis of symmetry of the chamber themselves (Fig. S3†). The electrodes, put 1 cm apart, were connected to a custom electrical stimulator[49]

allowing different voltages (0–23 V) and frequencies (1–10 Hz) to be imposed on the constructs with a square wave (2 ms duration).

Contractile functionality of at least $N = 3$ biologically independent constructs per condition was assessed by acquiring videos of their response to external electrical stimulation in bright field. Specifically, two parameters were evaluated: the excitation threshold (ET), defined as the minimum voltage (per cm) required to achieve synchronous beating of the whole constructs at a pacing frequency of 1 Hz, and the maximum capture rate (MCR), defined as the maximum imposed beating frequency a construct is capable of following with a stimulation voltage of 1.5 times the ET. Videos were acquired with an inverted microscope (Olympus IX81, 10× objective) equipped with a thermo-controlled chamber (CO_2 at 5% and temperature at 37 °C) and captured with a sampling frequency of 20 frames per second (CCD camera/DP30BW). Three areas of interest for each condition were further analysed.

Motion tracking analysis

Motion of cells was recorded only when constructs' synchronous beating was detected after electrical pacing was applied (*i.e.*, for high-CM and medium-CM conditions). For each recorded movie ($N = 2$ at least for each experimental condition), at least 3 regions-of-interest (ROI) were chosen and a minimum number of 5 different single cells were identified to track their motion with respect to adequate reference points during three entire contraction cycles (Fig. 7d). Accordingly, the entire contraction trajectory of each single cell was calculated manually, collecting the image coordinates of the cells at each photogram using Image J software. The variation of the position vector magnitude (referencing to the frame origin) was plotted against time to quantify the contraction frequency and compare it with the pacing frequency. For each trajectory of contraction, the contraction direction was calculated as the linear-regression angular coefficient tangent of the tracked cell coordinate cloud (*i.e.*, angle created between the direction and horizontal axis of the frame, Fig. 7b). Ultimately, for each analysed ROI the probability density function (PDF) of the contraction direction was estimated non-parametrically by a kernel smoothing estimation function (MATLAB 2018b, Mathworks), in order to quantify and identify the most probable contraction direction within each ROI. For each video two parameters were evaluated: (i) synchronicity of contractions peaks in each cell and (ii) the most probable cell contraction direction within the recorded ROI.

Statistical analysis

All data were presented as mean ± standard deviation. Statistical analyses were performed using Prism 8 (GraphPad). Population normality was assumed when both Shapiro–Wilk and Kolmogorov–Smirnov tests gave a positive result. Double comparisons were performed using a two tailed *t*-test for Gaussian populations and the Mann–Whitney test for non-Gaussian ones. Multiple comparisons were realized using one-way ANOVA with Dunnett's or Tukey's *post hoc* test for Gaussian populations and the Kruskal–Wallis test with Dunn's *post hoc* test for non-Gaussian populations. One sample *t*-test or Wilcoxon signed rank test was adopted to assess differences between a sample population, Gaussian or not respectively, and a theorical value. Statistical significance was indicated by $*p < 0.05$, $**p < 0.01$, $***p < 0.001$ and $****p < 0.0001$.

Author contributions

A. Marsano and M. Rasponi conceived the project. M. Rasponi., F. Carminati, A. Mainardi and G. S. Ugolini conceived the device. A. Mainardi and F. Carminati produced the devices. A. Mainardi, F. Carminati and G. S. Ugolini performed the mechanical characterization of the device. A. Mainardi, F. Carminati, P. Occhetta and G. Isu performed the biological experiments. G. Reid and R. Visone isolated primary cells. A. Mainardi, F. Carminati, D. R. Diaz, G. Isu and P. Occhetta performed biological analyses. A. Mainardi, P. Occhetta, G. Reid, A. Marsano and M. Rasponi wrote the manuscript. All the authors discussed the results commented on the manuscript and contributed to its final version.

Conflicts of interest

The authors declare no conflict of interest.

Acknowledgements

Device manufacturing was partially performed at PoliFAB—the micro- and nanofabrication facility of Politecnico di Milano. This work was supported by grants provided by Swiss National Science Foundation (310030_172989) to A. Marsano.

References

1 J. C. Deddens, A. H. Sadeghi, J. Hjortnaes, L. W. van Laake, M. Buijsrogge and P. A. Doevendans, *et al.*, Modeling the Human Scarred Heart In Vitro: Toward New Tissue Engineered Models, *Adv. Healthcare Mater.*, 2017, **6**(3), 1600571, DOI: 10.1002/adhm.201600571.

2 J. G. Travers, F. A. Kamal, J. Robbins, K. E. Yutzey and B. C. Blaxall, Cardiac Fibrosis: The Fibroblast Awakens, *Circ. Res.*, 2016, **118**(6), 1021–1040. Available from: http://www.ncbi.nlm.nih.gov/pubmed/26987915.

3 J. J. Tomasek, G. Gabbiani, B. Hinz, C. Chaponnier and R. A. Brown, Myofibroblasts and mechano: Regulation of connective tissue remodelling, *Nat. Rev. Mol. Cell Biol.*, 2002, **3**, 349–363.

4 H. Zhao, X. Li, S. Zhao, Y. Zeng, L. Zhao and H. Ding, *et al.*, Microengineered in vitro model of cardiac fibrosis through modulating myofibroblast mechanotransduction, *Biofabrication*, 2014, **6**(4), 045009, DOI: 10.1088/1758-5082/6/4/045009.

5 N. Nagaya, T. Fujii, T. Iwase, H. Ohgushi, T. Itoh and M. Uematsu, *et al.*, Intravenous administration of mesenchymal stem cells improves cardiac function in rats with acute myocardial infarction through angiogenesis and myogenesis, *Am. J. Physiol.*, 2004, **287**(6), 56–66.

6 J. M. Edelberg, S. H. Lee, M. Kaur, L. Tang, N. M. Feirt and S. McCabe, *et al.*, Platelet-derived growth factor-AB limits the extent of myocardial infarction in a rat model: Feasibility of restoring impaired angiogenic capacity in the aging heart, *Circulation*, 2002, **105**(5), 608–613.

7 S. Park, N. B. Nguyen, A. Pezhouman and R. Ardehali, Cardiac fibrosis: potential therapeutic targets, *Transl. Res.*, 2019, **209**, 121–137.

8 A. Leask, Potential therapeutic targets for cardiac fibrosis: TGFβ, angiotensin, endothelin, CCN2, and PDGF, partners in fibroblast activation, *Circ. Res.*, 2010, **106**, 1675–1680, DOI: 10.1161/CIRCRESAHA.110.217737.

9 V. Rai, P. Sharma, S. Agrawal and D. K. Agrawal, Relevance of mouse models of cardiac fibrosis and hypertrophy in cardiac research, *Mol. Cell. Biochem.*, 2017, **424**, 123–145.

10 J. Pellman, J. Zhang and F. Sheikh, Myocyte-fibroblast communication in cardiac fibrosis and arrhythmias: Mechanisms and model systems, *J. Mol. Cell. Cardiol.*, 2016, **94**, 22–31, DOI: 10.1016/j.yjmcc.2016.03.005.

11 A. H. Sadeghi, S. R. Shin, J. C. Deddens, G. Fratta, S. Mandla and I. K. Yazdi, *et al.*, Engineered 3D Cardiac Fibrotic Tissue to Study Fibrotic Remodeling, *Adv. Healthcare Mater.*, 2017, **6**(11), 1601434, DOI: 10.1002/adhm.201601434.

12 P. Occhetta, G. Isu, M. Lemme, C. Conficconi, P. Oertle and C. Räz, *et al.*, A three-dimensional: In vitro dynamic micro-tissue model of cardiac scar formation, *Integr. Biol.*, 2018, **10**(3), 174–183.

13 M. Kong, J. Lee, I. K. Yazdi, A. K. Miri, Y. D. Lin, J. Seo, Y. S. Zhang, A. Khademhosseini and S. R. Shin, Cardiac Fibrotic Remodeling on a Chip with Dynamic Mechanical Stimulation, *Adv. Healthcare Mater.*, 2019, **8**(3), e1801146, DOI: 10.1002/adhm.201801146.

14 C. M. Kofron and U. Mende, In vitro models of the cardiac microenvironment to study myocyte and non-myocyte crosstalk: bioinspired approaches beyond the polystyrene dish, *J. Physiol.*, 2017, **595**(12), 3891–3905, DOI: 10.1113/JP273100.

15 Y. Li, H. Asfour and N. Bursac, Age-dependent functional crosstalk between cardiac fibroblasts and cardiomyocytes in a 3D engineered cardiac tissue, *Acta Biomater.*, 2017, **55**, 120–130.

16 H. Zhang, L. Tian, M. Shen, C. Tu, H. Wu and M. Gu, *et al.*, Generation of quiescent cardiac fibroblasts from human induced pluripotent stem cells for in vitro modeling of cardiac fibrosis, *Circ. Res.*, 2019, **125**(5), 552–566. Available from: https://pubmed.ncbi.nlm.nih.gov/31288631/.

17 A. C. C. van Spreeuwel, N. A. M. Bax, B. J. van Nierop and A. Aartsma-Rus, Goumans MJTH, Bouten CVC. Mimicking Cardiac Fibrosis in a Dish: Fibroblast Density Rather than Collagen Density Weakens Cardiomyocyte Function, *J. Cardiovasc. Transl. Res.*, 2017, **10**(2), 116–127. Available from: https://pubmed.ncbi.nlm.nih.gov/28281243/.

18 S. Kumar, G. Wang, N. Zheng, W. Cheng, K. Ouyang and H. Lin, *et al.*, HIMF (Hypoxia-Induced Mitogenic Factor)-IL (Interleukin)-6 Signaling Mediates Cardiomyocyte-Fibroblast Crosstalk to Promote Cardiac Hypertrophy and Fibrosis, *Hypertension*, 2019, **73**(5), 1058–1070. Available from: http://www.ncbi.nlm.nih.gov/pubmed/30827145.

19 C. E. Rupert, T. Y. Kim, B. R. Choi and K. L. K. Coulombe, Human Cardiac Fibroblast Number and Activation State Modulate Electromechanical Function of hiPSC-Cardiomyocytes in Engineered Myocardium, *Stem Cells Int.*, 2020, **2020**, 9363809, DOI: 10.1155/2020/9363809.

20 P. Occhetta, A. Mainardi, E. Votta, Q. Vallmajo-Martin, M. Ehrbar, I. Martin, A. Barbero and M. Rasponi, Hyperphysiological compression of articular cartilage induces an osteoarthritic phenotype in a cartilage-on-a-chip model, *Nat. Biomed. Eng.*, 2019, **3**(7), 545–557, DOI: 10.1038/s41551-019-0406-3.

21 C. P. Huang, J. Lu, H. Seon, A. P. Lee, L. A. Flanagan and H. Y. Kim, *et al.*, Engineering microscale cellular niches for three-dimensional multicellular co-cultures, *Lab Chip*, 2009, **9**(12), 1740–1748.

22 A. Marsano, C. Conficconi, M. Lemme, P. Occhetta, E. Gaudiello and E. Votta, *et al.*, Beating heart on a chip: a novel microfluidic platform to generate functional 3D cardiac microtissues, *Lab Chip*, 2016, **16**(3), 599–610.

23 O. Mastikhina, B. U. Moon, K. Williams, R. Hatkar, D. Gustafson and O. Mourad, *et al.*, Human cardiac fibrosis-on-a-chip model recapitulates disease hallmarks and can serve as a platform for drug testing, *Biomaterials*, 2020, **233**, 119741.

24 V. Van Duinen, A. Van Den Heuvel, S. J. Trietsch, H. L. Lanz, J. M. Van Gils and A. J. Van Zonneveld, *et al.*, 96 perfusable blood vessels to study vascular permeability in vitro, *Sci. Rep.*, 2017, **7**(1), 1–11.

25 J. A. Boos, P. M. Misun, A. Michlmayr, A. Hierlemann and O. Frey, Microfluidic Multitissue Platform for Advanced Embryotoxicity Testing In Vitro, *Adv. Sci.*, 2019, **6**(13), 1900294, DOI: 10.1002/advs.201900294.

26 O. Schneider, L. Zeifang, S. Fuchs, C. Sailer and P. Loskill, User-Friendly and Parallelized Generation of Human Induced Pluripotent Stem Cell-Derived Microtissues in a Centrifugal Heart-on-a-Chip, *Tissue Eng., Part A*, 2019, **25**(9–10), 786–798, DOI: 10.1089/ten.tea.2019.0002.

27 S. J. Trietsch, G. D. Israëls, J. Joore, T. Hankemeier and P. Vulto, Microfluidic titer plate for stratified 3D cell culture, *Lab Chip*, 2013, **13**(18), 3548. Available from: http://xlink.rsc.org/?DOI=c3lc50210d.

28 R. Visone, G. S. Ugolini, V. Vinarsky, M. Penati, A. Redaelli and G. Forte, *et al.*, A Simple Vacuum-Based Microfluidic Technique to Establish High-Throughput Organs-On-Chip and 3D Cell Cultures at the Microscale, *Adv. Mater. Technol.*, 2018, 1800319, DOI: 10.1002/admt.201800319.

29 A. Redaelli, M. Rasponi and P. Occhetta, WO2016174607A1 - Microfluidic device and relative method for the generation and/or culture and/or maturation of three- dimensional cell and/or tissue constructs - Google Patents, [cited 2020 Feb 8]. Available from: https://patents.google.com/patent/WO2016174607A1/en.

30 R. Mohan, B. R. Schudel, A. V. Desai, J. D. Yearsley, C. A. Apblett and P. J. A. Kenis, Design considerations for elastomeric normally closed microfluidic valves, *Sens. Actuators, B*, 2011, **160**(1), 1216–1223.

31 N. G. Frangogiannis, Regulation of the inflammatory response in cardiac repair, *Circ. Res.*, 2012, **110**, 159–173.

32 N. Bildyug, E. Bozhokina and S. Khaitlina, Contribution of α-smooth muscle actin and extracellular matrix to the in vitro reorganization of cardiomyocyte contractile system, *Cell Biol. Int.*, 2016, **40**(4), 472–477, DOI: 10.1002/cbin.10577.

33 C. Jourdan-LeSaux, J. Zhang and M. L. Lindsey, Extracellular matrix roles during cardiac repair, *Life Sci.*, 2010, **87**, 391–400.

34 R. Kerkelä, J. Ulvila and J. Magga, Natriuretic peptides in the regulation of cardiovascular physiology and metabolic events, *J. Am. Heart Assoc.*, 2015, **4**, 2423. Available from: https://www.ncbi.nlm.nih.gov/pmc/articles/PMC4845118/.

35 D. Huh, B. D. Matthews, A. Mammoto, M. Montoya-Zavala, H. Yuan Hsin and D. E. Ingber, Reconstituting organ-level lung functions on a chip, *Science*, 2010, **328**(5986), 1662–1668.

36 A. Bein, W. Shin, S. Jalili-Firoozinezhad, M. H. Park, A. Sontheimer-Phelps and A. Tovaglieri, *et al.*, Microfluidic Organ-on-a-Chip Models of Human Intestine, *Cell. Mol. Gastroenterol. Hepatol.*, 2018, **5**, 659–668.

37 A. Herland, B. M. Maoz, D. Das, M. R. Somayaji, R. Prantil-Baun and R. Novak, *et al.*, Quantitative prediction of human pharmacokinetic responses to drugs via fluidically coupled vascularized organ chips, *Nat. Biomed. Eng.*, 2020, 1–16.

38 O. Schneider, L. Zeifang, S. Fuchs, C. Sailer and P. Loskill, User-Friendly and Parallelized Generation of Human Induced Pluripotent Stem Cell-Derived Microtissues in a Centrifugal Heart-on-a-Chip, *Tissue Eng., Part A*, 2019, **25**(9–10), 786–798, DOI: 10.1089/ten.tea.2019.0002.

39 C. Probst, S. Schneider and P. Loskill, High-throughput organ-on-a-chip systems: Current status and remaining challenges, *Curr. Opin. Biomed. Eng.*, 2018, **6**, 33–41.

40 C. M. Kofron and U. Mende, In vitro models of the cardiac microenvironment to study myocyte and non-myocyte crosstalk: bioinspired approaches beyond the polystyrene dish, *J. Physiol.*, 2017, **595**, 3891–3905. Available from: /pmc/articles/PMC5471366/.

41 D. Fan, A. Takawale, J. Lee and Z. Kassiri, Cardiac fibroblasts, fibrosis and extracellular matrix remodeling in heart disease, *Fibrog. Tissue Repair*, 2012, **5**(1), 15, DOI: 10.1186/1755-1536-5-15.

42 B. K. Podesser, M. Kreibich, E. Dzilic, D. Santer, L. Förster and S. Trojanek, *et al.*, Tenascin-C promotes chronic pressure overloadinduced cardiac dysfunction, hypertrophy and myocardial fibrosis, *J. Hypertens.*, 2018, **36**(4), 847–856.

43 R. Chiquet-Ehrismann, M. Tannheimer, M. Koch, A. Brunner, J. Spring and D. Martin, *et al.*, Tenascin-C expression by fibroblasts is elevated in stressed collagen gels, *J. Cell Biol.*, 1994, **127**(6 II), 2093–2101. Available from: /pmc/articles/PMC2120287/?report=abstract.

44 N. Shimojo, R. Hashizume, K. Kanayama, M. Hara, Y. Suzuki and T. Nishioka, *et al.*, Tenascin-C may accelerate cardiac fibrosis by activating macrophages via the integrin αVβ3/Nuclear Factor-κB/Interleukin-6 Axis, *Hypertension*, 2015, **66**(4), 757–766.

45 R. Visone, G. S. Ugolini, D. Cruz-Moreira, S. Marzorati, S. Piazza and E. Pesenti, *et al.*, Micro-electrode channel guide (μECG) technology: an online method for continuous electrical recording in a human beating heart-on-chip, *Biofabrication*, 2021, **13**(3), 035026.

46 C. O. Heras-Bautista, N. Mikhael, J. Lam, V. Shinde, A. Katsen-Globa and S. Dieluweit, *et al.*, Cardiomyocytes facing fibrotic conditions re-express extracellular matrix transcripts, *Acta Biomater.*, 2019, **89**, 180–192, DOI: 10.1016/j.actbio.2019.03.017.

47 M. Radisic, A. Marsano, R. Maidhof, Y. Wang and G. Vunjak-Novakovic, Cardiac tissue engineering using perfusion bioreactor systems, *Nat. Protoc.*, 2008, **3**(4), 719–738.

48 P. Chomczynski and N. Sacchi, Single-step method of RNA isolation by acid guanidinium thiocyanate-phenol-chloroform extraction, *Anal. Biochem.*, 1987, **162**(1), 156–159.

49 N. Tandon, C. Cannizzaro, P. H. G. Chao, R. Maidhof, A. Marsano and H. T. H. Au, *et al.*, Electrical stimulation systems for cardiac tissue engineering, *Nat. Protoc.*, 2009, **4**(2), 155–173.